

Enhanced Star Formation in Narrow Line Seyfert 1 AGN revealed by Spitzer

E. Sani^{1,2}, D. Lutz², G. Risaliti,^{3,4} H. Netzer⁵, L. C. Gallo⁶, B. Trakhtenbrot⁵, E. Sturm²,
T. Boller²

sani@arcetri.astro.it

ABSTRACT

We present new low resolution *Spitzer* mid-infrared spectroscopy of a sample of 20 ROSAT selected local Narrow Line Seyfert 1 galaxies (NLS1s). We detect strong AGN continuum in all and clear PAH emission in 70% of the sources. The 6.2 μm PAH luminosity spans three orders of magnitudes, from $\sim 10^{39}\text{erg s}^{-1}$ to $\sim 10^{42}\text{erg s}^{-1}$ providing strong evidence for intense ongoing star formation in the circumnuclear regions of these sources.

Using the IRS/*Spitzer* archive we gather a large number of additional NLS1s and their broad line counterparts (BLS1s) and constructed NLS1 and BLS1 subsamples to compare them in various ways. The comparison shows a clear separation according to FWHM($H\beta$) such that objects with narrower broad $H\beta$ lines are the strongest PAH emitters. We test this division in various ways trying to remove biases due to luminosity and aperture size. Specifically, we find that star formation activity around NLS1 AGN is larger than around BLS1 of the same AGN luminosity. The above result seems to hold over the entire range of distance and luminosity. Moreover the star formation rate is higher in low black hole mass and high L/L_{Edd} systems indicating that black hole growth and star formation are occurring simultaneously.

Subject headings: galaxies: active - galaxies: starburst - infrared: galaxies

¹Dipartimento di Astronomia, Università di Firenze, Largo E. Fermi 2, I-50125 Firenze, Italy

²Max-Planck-Institut für extraterrestrische Physik, Postfach 1312, 85741 Garching, Germany

³INAF - Osservatorio Astrofisico di Arcetri, Largo E. Fermi 5, I-50125 Firenze, Italy

⁴Harvard-Smithsonian Center for Astrophysics, 60 Garden Street, Cambridge, MA 02138

⁵School of Physics and Astronomy and the Wise Observatory, The Raymond and Beverly Sackler Faculty of Exact Sciences, Tel-Aviv University, Tel-Aviv 69978, Israel

⁶Department of Astronomy & Physics, Saint Mary's University, 923 Robie Street, Halifax, NS B3H 3C3, Canada

1. Introduction

The connection and co-evolution of active galactic nuclei (AGN) and star forming or starburst (SB) galaxies has become a major area of research. Understanding this evolution will supply most valuable information about the formation of the first black holes (BH), the accretion rate history and the growth of such systems through time, the building of galactic bulges, the metal enrichment of galaxies and clusters and more. Early studies (e.g. Rowan-Robinson 1995) suggested a possible common fueling mechanism for starburst galaxies and quasars. There is mounting evidence that intense star formation and nuclear activity are often closely related. This is evident from direct optical and infrared (IR) observations of many AGNs, the tight relationship between central BH mass and bulge mass (or bulge stellar velocity dispersion; see Ferrarese & Merrit 2000, Gebhardt et al. 2000, Marconi & Hunt 2003) and also from the analysis of luminous sources such as ULIRGs where nuclear activity and intense star formation (SF) are happening at the same time (e.g., Genzel et al. 1998).

The long term interest in the properties of type-I AGNs with narrow broad emission lines (Narrow Line Seyfert 1 galaxies - NLS1s) is closely related to the above issues. Such systems were defined more than three decades ago (Zwicky et al. 1971) and have received much attention due to their unusual X-ray properties. They are normally defined by their optical spectra in particular the requirement that $\text{FWHM}(\text{H}\beta) \leq 2000 \text{ km s}^{-1}$ (Osterbrock & Pogge 1985). Some properties of NLS1 are definitely extreme among type-I AGNs: (I) their X-ray spectra are very steep showing the presence of a large soft X-ray excess (Boller et al. 1996). The X-ray slope defined by $N_{ph} \propto E^{-\Gamma}$, has photon spectral indices ranging from $\Gamma = 1$ to $\Gamma > 4$. The X-ray luminosity span the range $10^{42} - 10^{45} \text{ erg s}^{-1}$. (II). They exhibit rapid, large amplitude X-ray variability (Gallo et al. 2004 and references therein). (III). Their optical FeII lines are very strong compared with $\text{H}\beta$ (Grupe et al. 2004). (IV). They show indications for large metal abundance in optical/IR (Shemmer & Netzer 2002, Shemmer et al. 2004) and X-ray (Tanaka et al. 2004, Fabian et al. 2009). Other extreme properties have been noted too. For example, Peterson and collaborators (2000) proposed that NLS1s have lower black hole (BH) masses compared with broad line Seyfert 1 galaxies (hereafter BLS1s) of similar luminosity. Translating their accretion rate and BH mass to L/L_{Edd} one finds that they are at the high end of the AGN distribution showing $L/L_{\text{Edd}} \simeq 1$ (see also Boroson 2002; Grupe 2004 and references therein). As such, they have been considered in several papers to be in the phase of building up their central BH (Mathur et al. 2001; Grupe & Mathur 2004).

The large accretion rate and high metallicity of NLS1s are likely related to the presence of active star forming regions in the hosts of such sources and Mathur (2000) suggested that

NLS1s live in rejuvenated, gas-rich galaxies with ongoing star-formation. This has been speculated in several individual sources with an ULIRG infrared nature (e.g. Tacconi et al. 2002; Risaliti et al. 2006) but has not been shown to be the case in large NLS1s samples.

In the present work, we want to obtain a detailed mid-infrared (MIR) spectroscopic characterization of circumnuclear regions in the hosts of NLS1s. The aims are to investigate the possibility that such hosts show more intense star formation compared with other AGNs and to check the various relationships between SF and BH accretion. The high sensitivity and resolution of the IRS spectrometer on board the *Spitzer Space Telescope* (Houck et al. 2004) provide a most suitable tool to achieve these goals by obtaining high S/N low resolution 5-15 μm spectra of many NLS1s. In particular we want to characterize the SF in such system using observations of polycyclic aromatic hydrocarbons (PAH) features that are superimposed on the strong MIR AGN continuum. The analysis of the SF-BH activity connection can then be carried out using a comparison sample of BLS1s of comparable luminosity.

This paper is organized as follows. The second section describes the NLS1 and BLS1 samples including the new *Spitzer* observations. In §3 we describe the data reduction and the analysis of the spectra which are a superposition of the spectra of the AGN and the star forming host. In §4 we use our samples to investigate in detail the differences between NLS1s and BLS1s and in §5 we summarize our results and list the most important conclusions. Throughout this paper we assume $H_0 = 70 \text{ km s}^{-1} \text{ Mpc}^{-1}$, $\Omega_M = 0.3$, $\Omega_\Lambda = 0.7$.

2. The sample selection

Our prime sample of 20 NLS1s is taken from a ROSAT sample of nearby AGN (Thomas et al. 1998), carefully characterized both in the optical (Grupe et al. 2004) and X-ray bands (Boller et al. 1996, Grupe et al. 2004) and not previously observed with *Spitzer* IRS. The *Spitzer* IRS observations of the new 20 NLS1s completing the sample are part of the PID 20241 program (PI D. Lutz).

All 20 sources considered here are of low redshift and only one (PHL 1092) has $z > 0.1$. The FeII line strengths range from $\text{FeII}/\text{H}\beta=0.1$ to $\text{FeII}/\text{H}\beta=3$, the soft X-ray slope is in the range $1 < \Gamma < 4$, and BH masses and X-ray luminosities span more than three order of magnitudes. These are some of the best studied NLS1s, permitting us to compare our MIR observations with other multi-wavelength properties of the sources. All our targets are relatively bright in the far infrared (FIR) and are detected by the IRAS satellite with a 60 μm flux $0.2 \text{ Jy} < S_{60} < 7 \text{ Jy}$. About 2/3 are detected at 12 μm with flux greater than

0.1 Jy.

The new data described here were supplemented by a large number of additional *Spitzer* archival spectroscopic observations of NLS1s and BLS1s. These were selected as follows: We first extracted all the NLS1s and BLS1s from the 12th edition of the Catalog of Quasars and Active Nuclei compiled by Véron-Cetty & Véron (2006, hereafter VQC06), using both catalogs of faint (i.e. Seyfert galaxies fainter than absolute magnitude $M = -23$) and bright AGNs (i.e. quasars brighter than $M = -23$). We probed for ‘S1n’ and for ‘S1’ or ‘S1.0’ or ‘S1.2’ classifications in VQC06, respectively. The defining criterion for inclusion as an NLS1 in the VQC06 is $\text{FWHM}(\text{H}\beta) \leq 2000 \text{ km s}^{-1}$. To assure high quality spectra, and to reduce aperture effects (see below) we used an upper redshift limit of $z \leq 0.2$. The final samples cover six orders of magnitude in luminosity. Among the BLS1s listed in VQC06, we excluded sources with Seyfert subclasses 1.5, 1.8 and 1.9. This is done to avoid confusion between NLS1s and BLS1s with particularly strong narrow lines, and possible intrinsic differences between Type 1 and Type 2 objects. We verified VQC06 spectral classifications from the literature or from SDSS DR7 spectra, eliminating a number of objects classified as S1 (1.0 or 1.2) in VQC06 but in fact corresponding to intermediate types lacking detectable BLR emission in $\text{H}\beta$.

Radio loudness is another potential bias. Synchrotron emission in radio loud (RL) AGNs can extend to shorter wavelengths and significantly contribute to the observed MIR continuum. This will dilute the hot-dust produced continuum and affect the relative strength of the observed PAH features. We therefore exclude RL sources from our sample.

The two lists thus defined were cross-checked against the Science Data Archive of the *Spitzer* Science Center (SSC) using the *Leopard* Archive Tool version 18.2 for selecting objects observed in the IRS Low Resolution Mode.

Table 1 shows the final samples together with their relevant optical properties and the observing log is in Table 2.

While cross-checking the catalogs and archives is generally very successful, there are definitely some exceptions and biases related to the way the catalog and archive proposals were produced. This makes it necessary to check the selection by hand. We checked a posteriori the optical classification of our sources considering $\text{FWHM}(\text{H}\beta)$. The $\text{H}\beta$ measurements are from various sources with literature references listed in Table 1 and our own measurements based on SDSS DR7 spectra and PG Quasar spectra (Boroson & Green 1992, and T. Boroson priv. comm.). As shown in Fig. 1 and Tab. 1 and 2, the sub-classification into the two groups is not precise. Indeed the NLS1s Mrk 291, Mrk 705, SDSS J131305.80+012755.9, IRAS 13349+2438, Mrk 734, PG 1402+261, PG 2130+099 show $\text{FWHM}(\text{H}\beta)$ which exceeds our limit of 2000 km s^{-1} . These sources show most of the well known extreme NLS1 prop-

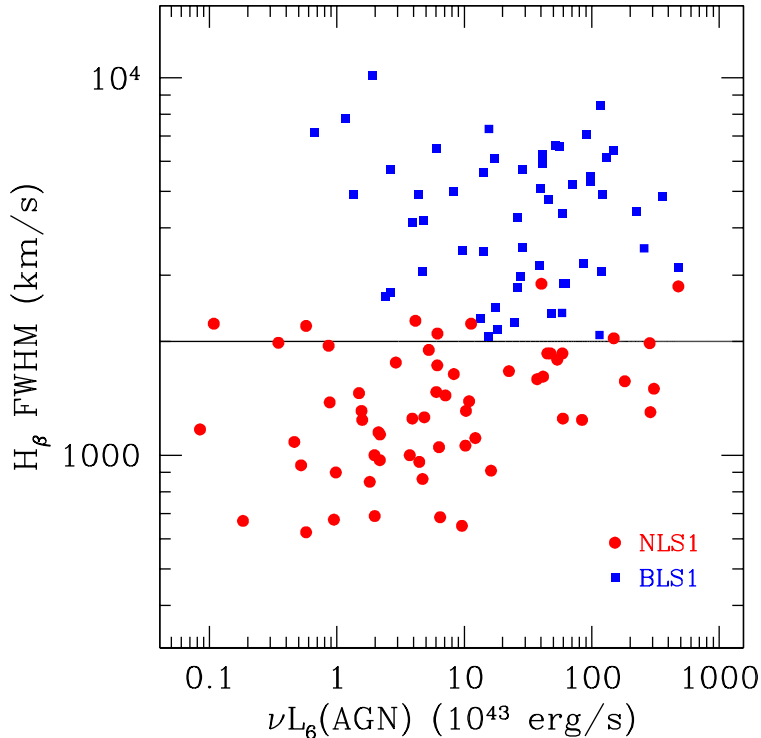


Fig. 1.— FWHM($H\beta$) - $L(6 \mu\text{m})$ plot for our sample. The observed $6 \mu\text{m}$ luminosities are computed as described in §3. BLS1s are marked with filled blue squares and NLS1s with red symbols. The threshold of 2000 km s^{-1} is also marked.

erties such as a steep soft X-ray slope and strong FeII lines. Indeed, all those sources are included in well known NLS1s samples such as Véron-Cetty et al. 2001, Boller et al. 1996, Zheng et al. 2002, Zhou et al. 2006 and Gallo et al. 2006. On the other hand, only sources with strictly $\text{FWHM}(H\beta) > 2000 \text{ km s}^{-1}$ are considered to build the broad line comparison sample. We note that several sources classified in the VCV06 catalog as type 1 and confirmed to have BLR $H\beta$ emission still show $\text{FWHM}(H\beta) \leq 2000 \text{ km s}^{-1}$. To be consistent, we move to the narrow line sample all the sources showing typical optical NLS1 signatures (i.e. spectra with $\text{FWHM}(H\beta) \leq 2000 \text{ km s}^{-1}$ and intense iron emission) also supported by published analysis (see Table 1 for detailed references). Examples of such cases are SDSS J131305.80+012755.9, SDSS J142748.28+050222.0, PG 1552+085.

3. Data reduction and analysis

The reduction and analysis described in this section have been applied to our new observations as well as to the archival data. This is done in order to ensure a consistent and uniform analysis. All data are low resolution ($\lambda/\Delta\lambda \sim 60 - 120$, long slit *Spitzer* IRS observations obtained in a staring mode (Houck et al. 2004)). We are interested in the rest frame wavelength range 5-14 μm , corresponding to the Short Low (SL) channel. The data reduction is carried out by applying our own IDL-based procedures starting with the two-dimensional basic calibrated data (BCD) provided by the version 17 of the *Spitzer* pipeline. We subtracted the sky by differencing, for each cycle, the two nod positions. In the difference thus computed, we replaced deviant pixels with values representative of their neighborhoods in the dispersion directions. In averaging all the cycles of the two-dimensional subtracted frames, we excluded values more than 2.5 times the local noise away from the mean. The calibrated one-dimensional spectra for the positive and negative beam were extracted using SMART (Higdon et al. 2004), and the two spectra averaged in order to obtain the final spectrum. Small multiplicative corrections were applied to take into account flux offset between the two low resolution orders. We also checked for consistency with the 12 μm and 25 μm IRAS fluxes when available, considering the possibility of aperture effects for nearby sources. The observation of Ton S180 represents a particular case. For the observation of this source the slit was not properly centered on the target due to adoption of an incorrect literature position. To properly calibrate the flux of this source we used the Long Low channel data (rest wavelength range 14-35 μm) and re-normalized the observed flux to the IRAS values. For this reason, we consider the Ton S180 measurements to be less reliable than the rest of the sample. Fig. 2 shows the final spectra of our 20 prime sources. We decomposed the AGN and star formation contribution to the observed spectrum by fitting the 5.5–6.85 μm rest wavelength range of the spectra with a simple model of a linear continuum representing thermal emission by AGN heated dust and a starburst template obtained from the ISO/SWS spectrum of M82. The latter is designed to enable a reliable measure of the 6.2 μm PAH emission feature in the spectrum. We note that the broad wavelength MIR spectrum of luminous AGNs (e.g. Schweitzer et al. 2006 (hereafter S06); Netzer et al. 2007) is well represented by a linear or power-law continuum over the limited wavelength range considered here.

The fit parameters obtained in this way were used to calculate the rest frame 6 μm pure AGN flux density and the 6.2 μm PAH flux. The latter is obtained by integrating over the rest wavelength range 6.1-6.35 μm . The detection criteria for both the AGN continuum and the 6.2 μm PAH feature are fixed at a 3σ level, and the error estimates are based on propagating the noise estimated from the difference of spectrum and fit over the rest wavelength range 5.5-6.85 μm . Cases of non-detections were assigned a 3σ continuum and/or PAH upper

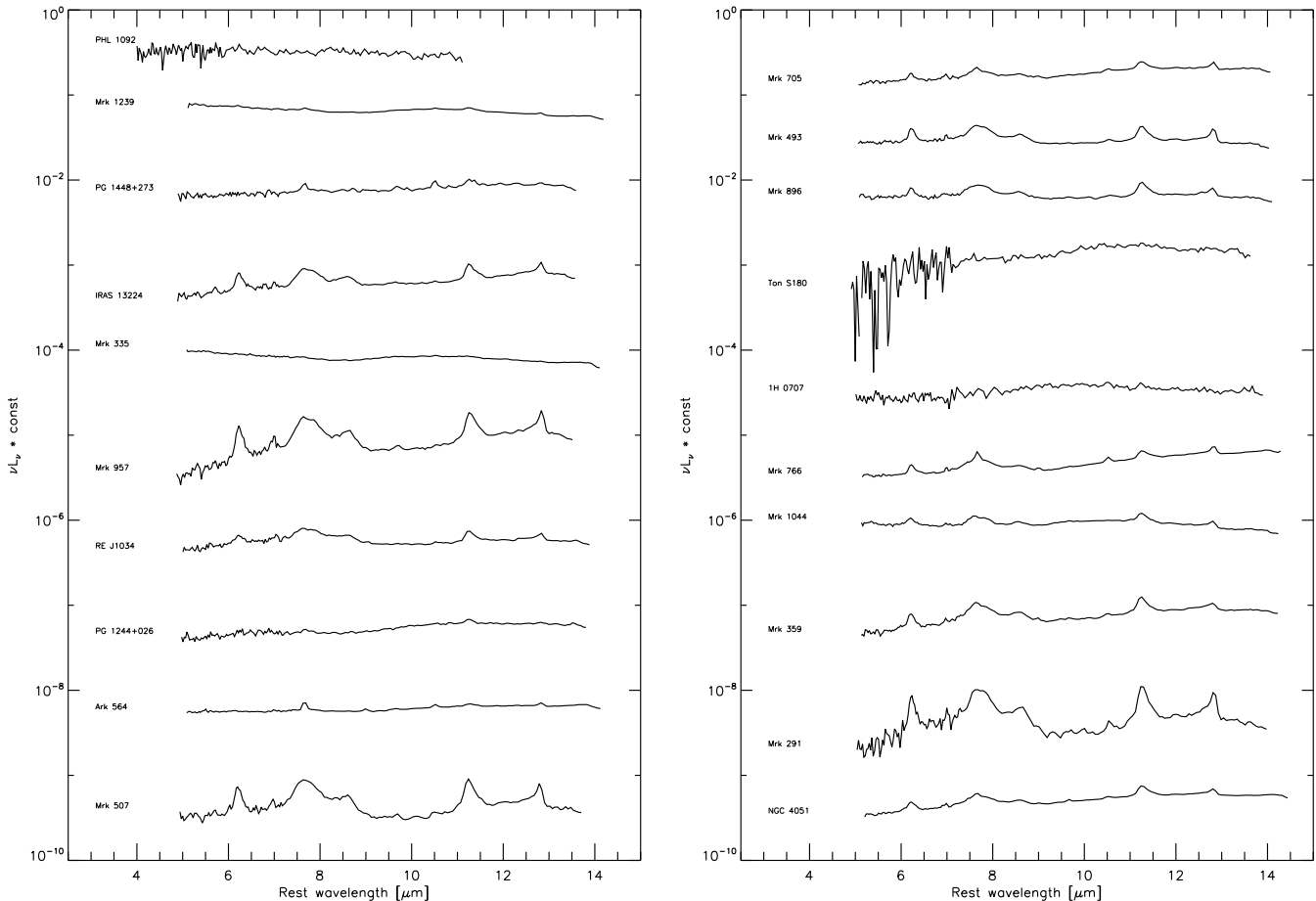


Fig. 2.— *Spitzer* IRS spectra for our prime NLS1 sample. The spectra are arbitrarily scaled for clarity, and are ordered with decreasing luminosity from the top left. These spectra are of high quality and high S/N, and are representative of the variety of NLS1 mid-IR spectral shapes.

limit. All fluxes were converted to luminosities which are referred to later on as $L(6\mu\text{m})$ and $L(6.2\text{ PAH})$. The only galaxy with a continuum upper limit is considered a non detection and is reported in the tables for completeness but is not considered in the analysis and discussion sections. The choice of the $6\mu\text{m}$ continuum enables to define in a clean way the hot-dust continuum produced by the dusty structure (torus) surrounding the AGN. This part of the spectrum is easy to measure and not much affected by strong emission or absorption features (e.g. S06). As for the PAH, we prefer to use the $6.2\mu\text{m}$ PAH feature, instead of the strong $7.7\mu\text{m}$ PAH emission feature, because it is not affected by blending with atomic lines such as [NeVI] and because its profile is not distorted by the $9.7\mu\text{m}$ silicate feature. The choice of

6.2 μm PAH causes nondetection in some weak PAH sources where other PAH features are seen, we consider this acceptable and justified by its other advantages. The continuum and PAH fluxes (luminosities) and upper limits are listed in Table 3 for the complete ROSAT and archival sample of 59 NLS1 (58 detections) and 54 BLS1s (all detected).

4. Results

The results of our analysis are shown in Table 3, Figures 3, 4, 6 and are summarized below:

- For the entire samples, the PAH features for star formation are detected with a 3σ significance in 70 % of NLS1s and 45 % of BLS1s.
- The comparison between unbiased NLS1 and BLS1 samples shows how the two population are separated and that NLS1s are related to a more intense SB activity than BLS1s. Possible luminosity and distance effects are carefully taken into account in the following discussion.

4.1. Mid-IR spectral properties

Our original sample of 20 sources is characterized by high quality and high S/N spectra, and can be considered representative of MIR spectral properties of the entire NLS1 sample. As one can infer from Fig. 2, and the dedicated part of Table 3, thanks to the high quality of our 20 spectra we are able to detect the 6.2 μm PAH feature in most of all the sources (14/20 of the prime sample).

From a visual inspection of Fig. 2, IRAS 13224-3809, Mrk 957, Mrk 507 and Mrk 291 show the most prominent PAH features. Indeed, among the known AGN these belong to the ones with the strongest SF signatures relative to the underlying AGN continuum (values in column 4 and 5 of Tab. 3, see below for details on R values).

There are only six (30% of the subsample) upper limits for the 6.2 PAH flux. Among these, three spectra (PHL 1092, Ton S180, 1H 0707-495) have a low S/N due to their large distance or intrinsic faintness and, in the case of Ton S180 pointing problems (see §3 for details), thus their upper limits are not very constraining (see the high values in Tab. 3 column 3). The other limits (Ark 564, Mrk 335, PG 1448+273) have high S/N spectra and the low limits values establish strong constraints for the detection of the 6.2 PAH. Nevertheless, the lack of this feature does not imply the complete absence of ongoing star formation as the it can be diluted by the strong AGN continuum (S06). The presence of 7.7, 11.3 and 12.7 PAH features strengthens this possibility, Mrk 335 being the only exception. The peculiar case

of Mrk 335 is discussed in Appendix together with two sources showing strong $9.7 \mu\text{m}$ silicate absorption and one strong star forming BLS1.

4.2. Star Formation activity vs. FWHM($\text{H}\beta$) for NLS1 and BLS1 galaxies

To quantify the contribution of star forming regions to the NLS1s and BLS1s spectra we define the SF-AGN ratio R by

$$R = \frac{L(6.2, PAH)}{\nu L_\nu(6, AGN)} \quad (1)$$

R is proportional to the PAH equivalent width (EW) measured against the pure AGN continuum. R values for the entire sample are listed in column 6 of Tab. 3, the correlation of R vs. FWHM($\text{H}\beta$) is plotted in the left panel of Fig. 3, while histograms in the right panel show the distribution of R for NLS1 and BLS1.

Visual inspection of Fig. 3 suggests that NLS1s are characterized by larger R which can be interpreted as a larger relative star formation contribution to their MIR spectra. In particular the histogram points out a greater PAH detection rate in NLS1 than BLS1, and, most of all that the majority of these detections correspond to the strongest circumnuclear SF activity ($R > 1$). On the other hand R values for BLS1 are mostly upper limits, and the detections typically lie in the intermediate R range ($0.1 < R < 1$).

This impression is substantiated by a formal censored statistics which we applied to the data. We used an improved version of the logrank test (Peto & Peto 1972), which correctly treats left-censored data. For the purpose of the analysis we divided the sample in two assuming in Fig. 3 a division line of FWHM($\text{H}\beta$) = 2000 km s^{-1} , and compare their properties with respect to R . This gave a negligible probability (6×10^{-5}) that the two sub-samples are drawn from the same parent distribution. Moving the dividing line up or down by 100 km s^{-1} did not change the conclusion. This significant difference between NLS1 and BLS1 groups indicates that type-I AGNs with narrower broad emission lines reside in hosts containing more luminous SF regions.

While the above is the main finding of the present paper, there are several potential effects that could bias this result and lower its significance. The ratio R could be small either due to dilution by the AGN continuum or or if the starburst is young (Rowan-Robinson & Efstathiou 2009). The last possibility can be traced by relating the $9.7 \mu\text{m}$ silicate strengths with the R values (similarly to Spoon et al. 2007). However, among our sample IRAS 11119+3257 and Mrk 231 are the only sources with strong silicate absorption, as shown in Fig. 10 and described in the Appendix for peculiar sources. Moreover, silicate emission

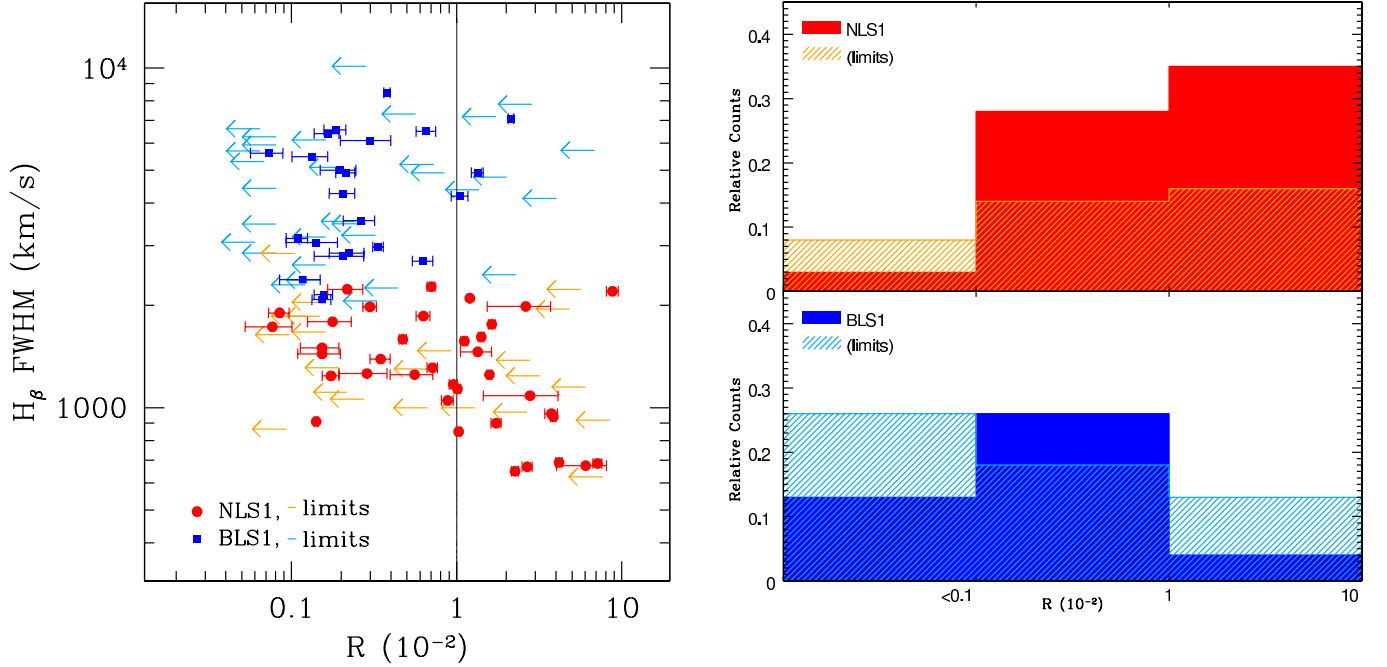


Fig. 3.— FWHM($H\beta$) vs the PAH to continuum ratio R (defined in §4.2, Eq. 1). Arrows indicate upper limits. Red dots are NLS1 whose upper limits are in orange. Blue squares are BLS1 with sky-blue limits. *Left panel:* the bidimensional plot displays the measurements and the black vertical line divides sources with strong SF ($R > 10^{-2}$) from the rest of the sample. *Right panel:* the R relative counts (limits) distribution is shown for both the NLS1 and BLS1 samples. The distribution is shown in bins for the three R orders of magnitude, relative to the proper sample number of sources.

is clearly detected in several sources (e.g. I Zw1, PG1211+143, PG0804+761 and others in both NLS1 and BLS1 samples), and well highlighted in the stacked spectra of Fig. 6. Thus, the possible contamination by young/obscured starbursts is mostly ruled out. The general issue of silicate emission and absorption features is the subject of a forthcoming paper including the present sample.

The two most important ones are aperture and luminosity effects. The first depends on the source distance and is the result of the fixed size *Spitzer* slit width that includes more host galaxy light in more distance sources. The IRS slit width is $3.6''$ for the spectral range used here, i.e 3.5 kpc at a typical distance of 200 Mpc. This can result in larger R (more PAH emission) at higher redshifts. The second potential bias is related to the well know increase in $L(\text{PAH})$ with AGN luminosity. The dependence of the two has been investigated in several samples (e.g. S06) and, while linear, the slope is not 1 which can introduce a trend of R with AGN luminosity. Our NLS1 and BLS1 samples were not chosen on the basis of their

similar distances or AGN luminosity thus the above may affect the trend seen in Fig. 3. The rest of this section addresses the above potential biases by comparing the two samples in various ways that are relevant to those effects.

4.3. Flux, luminosity and distance correlations

We have constructed two-dimensional diagrams combining observational (measured flux and distances) and deduced (luminosities and R values) properties of the sources in our two sub-samples. These correlations are shown in Fig. 4. The top left panel of the diagram examines the relation between the observed $6\mu\text{m}$ continuum and 6.2-PAH fluxes of our sources. NLS1s and BLS1s seem to be broadly separated. A region defined by $F(\text{PAH}) \gtrsim 1 \times 10^{-20} \text{ W cm}^{-2}$ holds mostly NLS1. The two BLS1s that are outside these limits are the ones with the strongest PAH, Mrk 231, and IRAS 13342+3932. Among these, Mrk 231 lies in the intermediate R values range of the histogram (Fig. 3), while IRAS 13342+3932 ($R \sim 2 \times 10^{-2}$) represents the only BLS1 with SF activity comparable with what is observed in NLS1. Mrk 231 and IRAS 13342+3932 are also discussed in the Appendix for peculiar sources. This separation strengthens the earlier suggestion of enhanced star formation activity, and the stronger PAH features in NLS1s, but may still be affected by aperture and luminosity effects.

Possible physical trends are examined in the top right panel of Fig. 4. This panel confirms that the earlier mentioned luminosity correlation between AGN continuum and star formation traced by PAH is also seen in our sample. Clearly $L(\text{PAH})$ increases with $L(6\mu\text{m})$ for the entire sample. The slope of the correlation (which is not necessarily identical to the slope found in S06 who used a sample of higher luminosity sources) is $L(\text{PAH}) \propto L(6\mu\text{m})^{0.7}$ i.e. sublinear.

The two bottom panels of the diagram examine the dependence of R on source luminosity and distance. The bottom left panel shows a clear decrease of R with $L(6\mu\text{m})$. This reflects the sublinear slope seen in the top right panel meaning that $L(6\mu\text{m})$ increases more rapidly than $L(\text{PAH})$. The two sub-classes are still separated in this diagram, in the sense that at given AGN luminosity the NLS1 populate regions of larger luminosity ratio, with considerable scatter. Again this is suggesting enhanced star formation around NLS1 AGN.

The bottom right panel of Fig. 4 is the one most relevant to the potential biases. Here R is plotted as a function of source distance which is translated to a larger physical aperture and increased host contribution. The diagram shows no particular trends suggesting that host galaxy contribution is not an important factor in determining R. The NLS1s-BLS1s separation in this plot is similar to the one seen in the other panels.

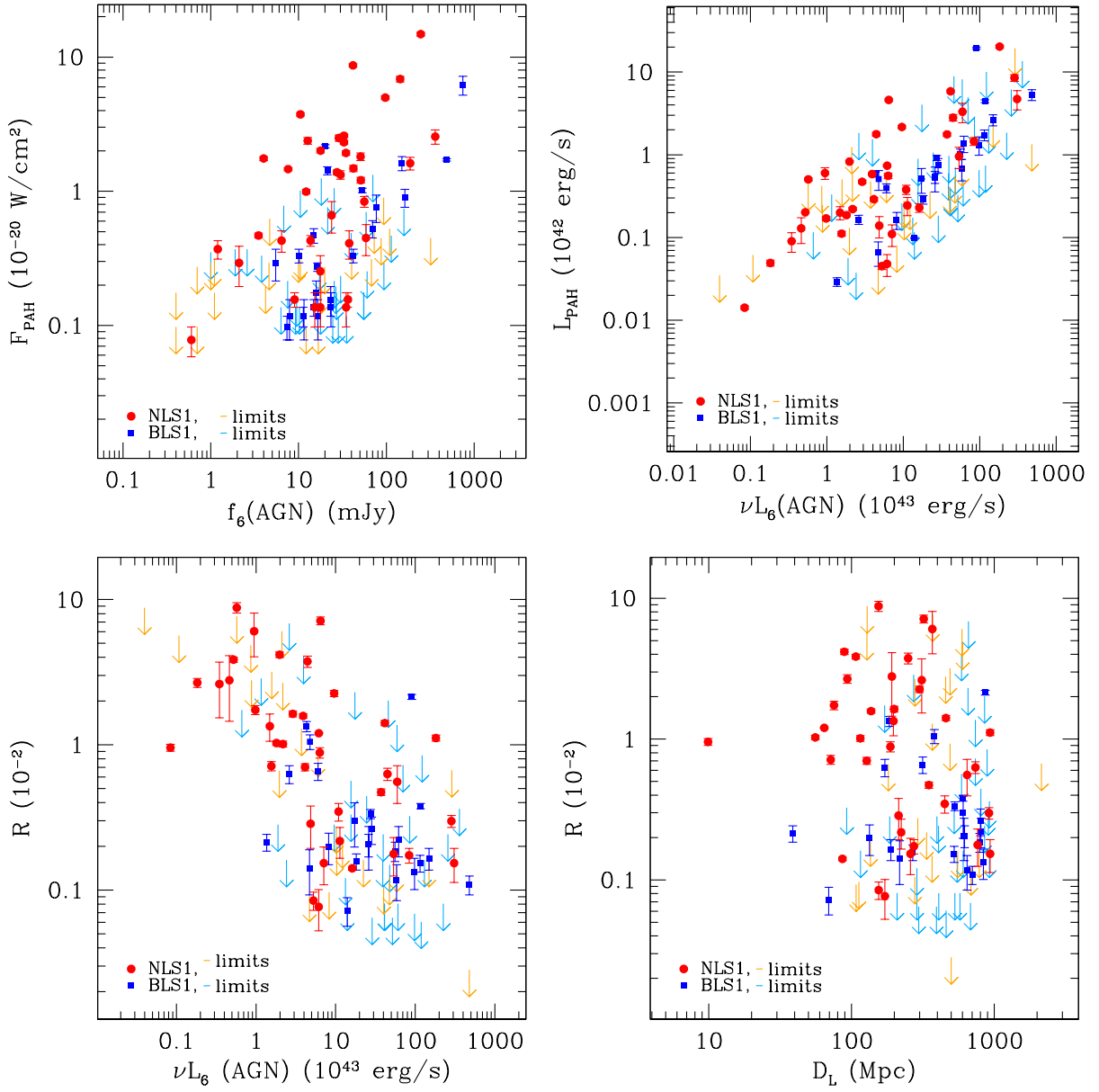


Fig. 4.— Correlation plots for NLS1 (red) and BLS1 (blue). Symbols are as in Fig. 3. Top left: $6.2 \mu\text{m}$ PAH flux as a function of $6 \mu\text{m}$ AGN flux. Top right: same as top left for luminosity. Bottom left: The luminosity ratio R as a function $L(6 \mu\text{m})$. Bottom right: R as a function of source distances.

In conclusion, the NLS1 and BLS1 AGNs investigated here seem to represent two groups of type-I sources that differ in their star formation properties. This does not resemble an

artifact of aperture or luminosity effects and seems to be an intrinsic property of the two subclasses. The important parameter separating the two groups is their measured $\text{FWHM}(\text{H}\beta)$ (Fig. 3). To further investigate the potential influence of source distance and luminosity

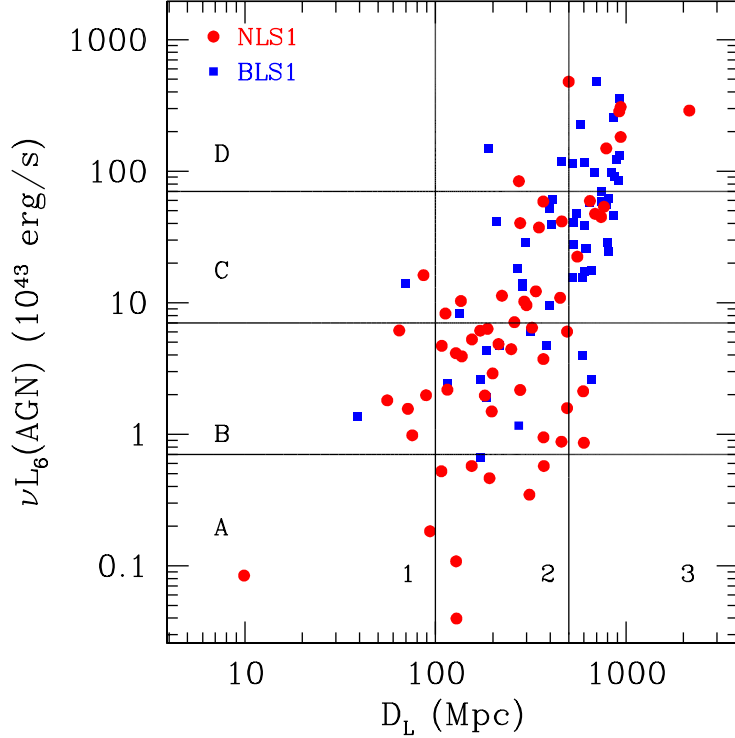


Fig. 5.— Luminosity-Distance diagram. The 10 regions shown are defined considering the AGN luminosity and redshift orders of magnitude.

on the R vs. $\text{FWHM}(\text{H}\beta)$ correlation in a way fully including the PAH nondetections, we have derived composite spectra of NLS1s and BLS1s in different luminosity-distance regimes. This was achieved by dividing the entire luminosity-distance space into ten regions defined by sampling the luminosity range in four equally spaced bins of the size of one order of magnitude, and the distance axis in three zones spacing the redshift range in bins of one order of magnitude each. This corresponds to distance thresholds of 100 and 500 Mpc and AGN luminosity limits of 7×10^{42} , 7×10^{43} and 7×10^{44} erg/s. The ten zones and the distribution of NLS1s and BLS1s in them are shown in Fig. 5. We then obtained stacked spectra of all the NLS1s in each zone and compared them with stacked spectra of all the BLS1s in the same zone. The spectral combination is achieved by shifting all spectra to zero redshift and by normalizing individual spectra to the same $6\mu\text{m}$ AGN continuum flux density. The purpose is to inspect visually the composite spectra in order to verify the previous conclusion that R is indeed larger in NLS1s once the luminosity and distance effects have been removed.

The final number of sources for each zone and the composite spectra are shown in Fig. 6. To compare quantitatively the star formation contributions of NLS1s and BLS1s in the same zone, we treated the composite spectra in the same way used to define R for individual sources. We then define a variable describing the relative importance of star formation in NLS1 compared to BLS1, F_{SB} by

$$F_{SB} = \frac{R_{NLS1}(PAH, 6.2)}{R_{BLS1}(PAH, 6.2)}, \quad (2)$$

where $R_{NLS1}(PAH, 6.2)$ and $R_{BLS1}(PAH, 6.2)$ are the ratios of 6.2 μm PAH fluxes to 6 μm AGN continuum (see Eq. 1) for the NLS1 and BLS1 average spectra, respectively. $F_{SB} > 1$ stands for a more intense SF activity in NLS1s compared to BLS1s. In Table 4 we list the measured values of R and F_{SB} in all ten zones. We emphasize that in all the bins but two, an enhanced NLS1 star formation activity is found by at least a factor $\gtrsim 2$. Only one zone (A1) is an exception hosting no BLS1 and is discussed below. A detailed account of the results of this analysis is in Appendix A (see Fig. 6 for a visual inspection). To summarize, in almost all ten zones defined by distance and AGN luminosity, star forming activity in NLS1 seems to be stronger, by our definition based on the relative strength of the 6.2 PAH emission feature in NLS1s. The three zones (A1, C1, D2) with poor statistics in both NLS1 and BLS1 require some caution. Nevertheless the small number of sources characterizing these zones is due to both physical and selection issues. Indeed, it is unexpected to find high luminosity sources (i.e. quasars) in the nearby Universe ($z < 0.02$). We also note an intrinsic bias for sources entering a literature based archival sample: using the $H\beta$ width as the prime selecting criterion we may preferentially miss faint BLS1 galaxies, because broad $H\beta$ will be harder to identify against the host continuum. Finally the very faint and distant sources will not have entered the sample because of observational limitations even with a sensitive instrument like *Spitzer*. However, thanks to the sufficient statistics in most of the zones (8/10), the main result of stronger star formation activity in NLS1 is preserved and is clearly indicated in our R vs. $\text{FWHM}(H\beta)$ correlation (see Fig.3). Also the combination of measured and deduced quantities for NLS1s and BLS1s (Fig. 4) robustly supports our finding.

As a further confirmation of our result, in Fig. 7 we have averaged the spectra of sources without a detection of the 6.2 μm PAH feature. A clear detection of the 6.2 μm PAH is present in the stacked spectra of both NLS1 and BLS1, and a more intense star formation activity occurs in narrow line Seyferts with an NLS1/BLS1 enhance factor of $F_{SB} = 2.6 \pm 0.5$. Concerning the possible luminosity and distance effects on the SF comparison factor, we do not find any peculiar trend. This can be inferred from both a visual inspection of different zones in Fig. 6, and by comparing R and F_{SB} values (Tab. 4) in terms of AGN luminosity and distance.

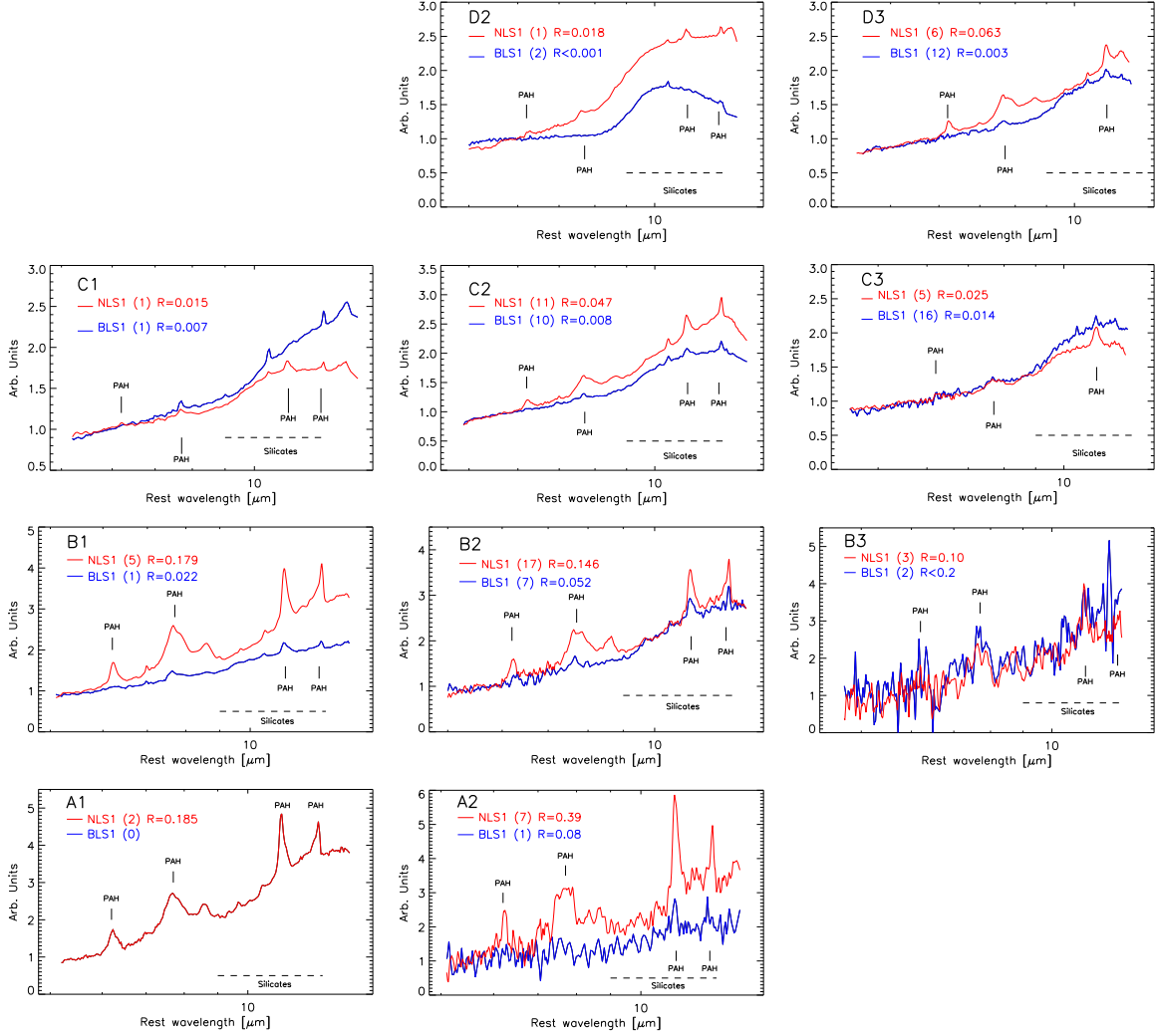


Fig. 6.— Average NLS1 spectra (red) compared with averaged BLS1 spectra (blue). The panels are arranged and labelled like the regions defined in the luminosity-distance diagram (Fig. 5). Each panels cites also the number of sources involved in the stacking procedure and the proper R values.

In particular, possible distance effect are crucial for the validity of our conclusion. As a further check we perform a distance stack by collapsing the luminosity bins in the luminosity-distance plot (Fig. 5) and grouping sources in the three distance zones. The mean distance-dependent spectra are shown in Fig. 8. Significant distance effects would imply an increase of the 6.2 PAH intensity with increasing redshift. This effect is not observed in both NLS1 and BLS1 mean spectra. On the contrary, a relatively fainter PAH emission found for the most

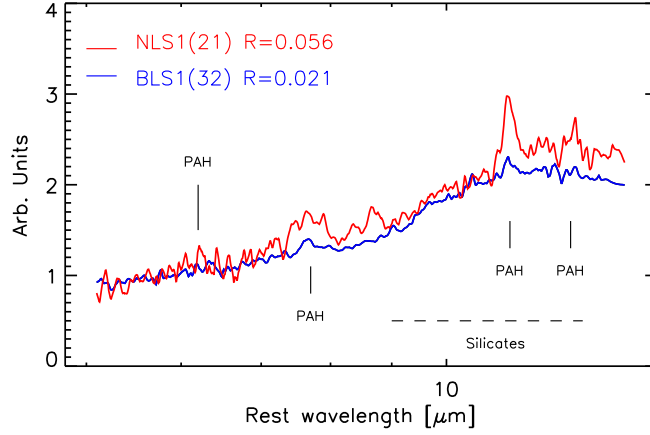


Fig. 7.— Stacked spectra for NLS1 (red) and BLS1 (blue) characterized by no $6.2\mu\text{m}$ PAH detection in the individual spectrum.

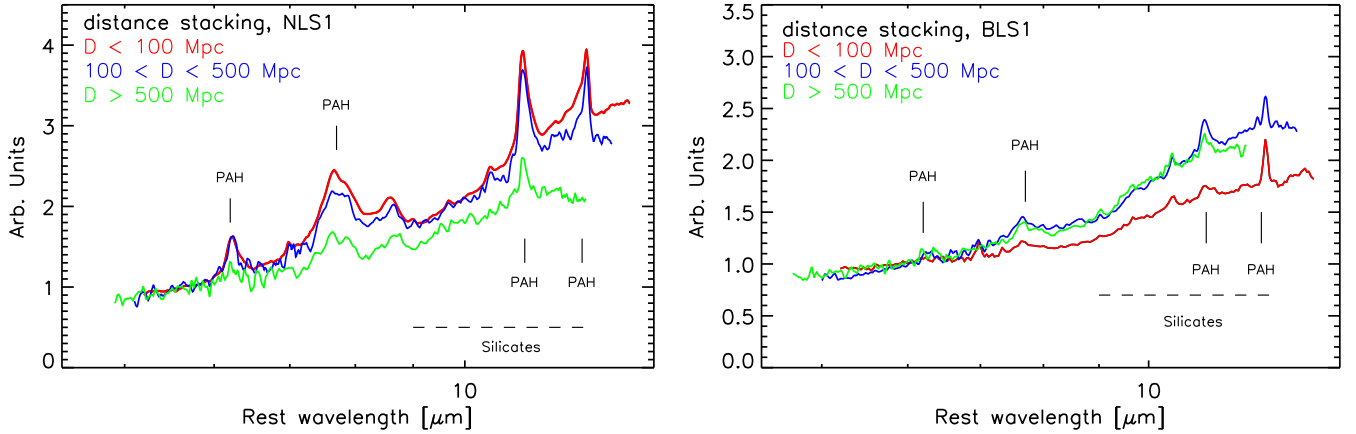


Fig. 8.— Stacked spectra for NLS1 (*left panel*) and BLS1 (*right panel*). The data have been grouped in the three distance zones (1, 2, 3) of Fig. 5.

distant ($D > 500$ Mpc) NLS1s. This can be plausibly ascribed to the higher AGN luminosity of these sources in combination with the sublinear increase of PAH luminosity with AGN luminosity (Fig. 4 top right). We note that, also for this grouping by distance only, NLS1 have stronger PAH.

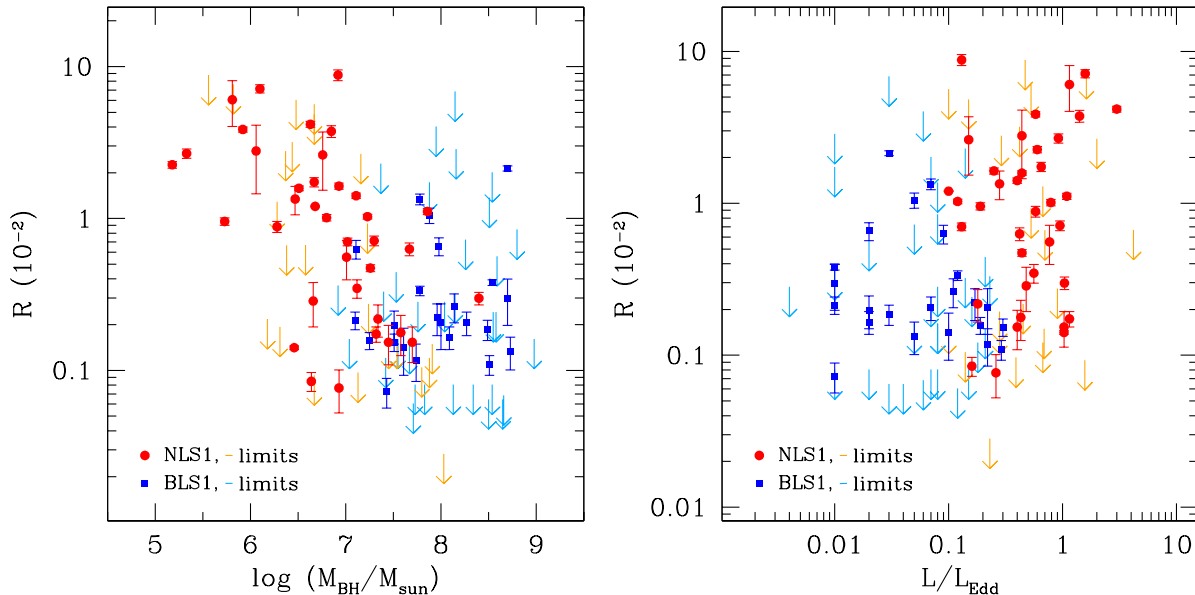


Fig. 9.— PAH-to-AGN continuum ratio R as a function of the central SMBH parameters. Symbols are as in Fig. 3. *Left panel*: R values versus central BH mass. *Right panel*: R values versus Eddington luminosity ratio. The BH masses and Eddington Ratios are computed according to Eq. 3 and 4 respectively (see text for details).

5. Discussion

In the previous section we have compared measured (flux and distance) and deduced (luminosity and R) parameters carefully taking into account luminosity and distance effects. A SF-AGN luminosity correlation has been seen and discussed in Netzer et al. (2007) and Lutz et al. (2008), and here we have confirmed this trend disentangling SF and AGN spectral components in the Spitzer short wavelength band. We have demonstrated an enhanced star formation activity in NLS1 galaxies compared to their broad line counterparts, and the enhancement factor (F_{SB}) does not appear to be affected by luminosity and distance effects.

In this section, we want to investigate a possible physical connection between the AGN fueling and star formation mechanisms. Such a connection has been proposed by several authors (i.e. Grupe & Mathur 2004, Shemmer et al. 2004, Komossa & Xu 2007 and references therein), but it has not been demonstrated by direct observational evidences. Here we compare the SF tracer with the AGN accretion parameters, that is, the 6.2 PAH luminosity -to- AGN continuum emission (R) is plotted as a function of the central black hole mass and Eddington ratio.

Black hole masses and accretion rates are computed by the single-epoch mass determination method based on the Kaspi et al. (2005) using the Broad Line Region size vs 5100\AA monochromatic luminosity ($R_{BLR}-\lambda L_{\lambda}(5100)$) relation. Thus, the BLR size is estimated from the measured $\lambda L_{\lambda}(5100)$ (col. 5 of Tab. 1), and the mass estimate follows from assuming Keplerian motion of the $H\beta$ emitting gas ($FWHM(H\beta)$) are in col. 4 of Tab. 1). The reverberation mapping-based scaling relations adopted here are (see Netzer and Trakhtenbrot 2007 - NT07 for more details):

$$M_{BH} = 1.05 \times 10^8 \left(\frac{L_{5100}}{10^{46} \text{erg/s}} \right)^{0.65} \left[\frac{FWHM(H\beta)}{1000 \text{ km/s}} \right]^2 M_{\odot} \quad (3)$$

and

$$L/L_{Edd} = \frac{f L_{5100}}{1.5 \times 10^{38} [M_{BH}/M_{\odot}]} \quad (4)$$

for BH mass and accretion rate respectively and where L_{5100} stands for the 5100\AA monochromatic luminosity. In this equation f is the bolometric correction factor. For low to intermediate luminosity AGN, this factor is between 7 and 12 (Marconi et al. 2004, Netzer 2009) and is possibly luminosity dependent. Hence, bolometric luminosities were calculated from the monochromatic luminosities (L_{5100}), by using the correction factors of Marconi et al. (2004). These M_{BH} (and thus L/L_{Edd}) values are considered to be accurate to within a factor of $\sim 2 - 3$ (see, e.g. Vestergaard & Peterson 2006).

Figure 9 displays the bi-dimensional SF vs AGN properties plots. As seen in the left panel of this figure the star formation activity increases with decreasing BH masses, and moreover the region of low BH masses and highest R values ($\text{Log}(M_{BH}/M_{\odot}) < 7$ and $R \gtrsim 10^{-2}$) is populated by NLS1s with the complete absence of BLS1s. Another interesting behavior is found also in the Fig.9 right panel, where the R value increases with the Eddington ratio, i.e. the AGN luminosity expressed in terms of the Eddington luminosity. Also in this case NLS1s are the only AGNs populating the region of the extreme measurements of both SF activity and Eddington ratio.

The upper limits in R make us refrain from expressing this trend in terms of a quantitative scaling relation between star formation activity and Eddington ratio. Nevertheless, our plots demonstrate the supposed intimate correlation between the circumnuclear (within few central kpc) star formation and the AGN fueling.

The NLS1 galaxies are characterized by smaller BH mass, larger Eddington ratio and stronger SF activity compared to their broad line counterparts. Thus, we can safely conclude that AGN with the higher accretion efficiency are surrounded by more intense star formation than the less violently accreting SMBHs in the local Universe.

This SF-AGN correlation is possibly driven by a feedback process between the two. Chen et al. (2009) have recently traced the star formation history of the circumnuclear regions in

type 2 AGNs, and proposed a model in which supernova explosions play a key role in the transportation of gas to galactic centers. Other works (i.e Silk & Rees 1998, Di Matteo et al. 2005) propose that AGN energetic outflows may affect the star formation in protogalaxies. While our work establishes a connection between star formation and accretion rate, we cannot draw definitive conclusions on its causal link to such feedback or feeding mechanisms. Shemmer et al. (2004) demonstrated that NLS1s are also the local Universe representatives of the objects with high accretion rate (L/L_{Edd}) and high metallicity in the metallicity - accretion rate relationship for AGNs. Again this relation suggests an intimate connection between Starburst enriching the circumnuclear gas and AGN fueling, represented by the accretion rate. Because we demonstrate that the efficient SMBH growth in NLS1 is associated with the most active circumnuclear SF regions, we can only support the previous finding in an indirect way. Indeed the metallicity inferred by Shemmer and coauthors refer to the AGN broad line region, while the star forming activity investigated in our work happens in much larger regions.

From an evolutionary point of view, a high star formation efficiency is necessary for a rapid BH growth in high redshift systems (Kawakatu & Wada 2009). Thus, assuming NLS1s as the early phase of BLS1s, our results would confirm the above model predictions. The local nature of our sources and the observable analyzed here can not directly confirm this evolutionary path, though our observations are an intriguing starting point for further high redshift investigations.

6. Conclusions

We have analyzed low resolution 5-15 μ m spectra of NLS1 and BLS1 galaxies obtained with the *Spitzer* IRS spectrometer. Thanks to the high spatial resolution and sensitivity of the instrument we have determined AGN 6 μ m continuum and 6.2 μ m PAH luminosities.

From the comparison of observed and derived quantities (in particular the SF-to-AGN ratio) we find a more intense circumnuclear SF activity in NLS1s than in their broad line counterparts (Fig. 3). Possible luminosity and distance effect of this enhanced activity have been carefully taken into account by using both bi-dimensional diagrams (Fig.4) and stacking procedures (Fig. 6, 8). No trends affecting our main conclusion have been found.

Our paper shows yet another way to distinguish NLS1s from broader line AGNs. This is another clear indication (on top of the extreme X-ray properties) that emission line widths are indeed related to fundamental physical properties, in the case under study the properties of the host galaxies.

Finally, we have estimated the BH mass and accretion rate (Eq. 3, 4) and plotted the SF-to-AGN ratio R as a function of these. Figure 9 shows that NLS1s hosting more violently

accreting BH also harbor more intense circumnuclear star formation.

7. Appendix A: stacked spectra

The following is a detailed comparison of the NLS1 and BLS1 stacked spectra shown in Fig. 6.

Zone A1, $D_L < 100$ Mpc, $\nu L_\nu(\mathbf{6,AGN}) < 7 \times 10^{42}$ erg/s. These are nearby objects and the numbers are small with only 2 NLS1s and no BLS1s, thus preventing us from direct NLS1-BLS1 comparison for nearest and less luminous object. The absence of BLS1 sources is not surprising, indeed with such faint sources the detection of a broad $H\beta$ feature turns to be difficult due to the spread of the few revealed photons over a relatively large wavelength range.

Zone A2: $100 < D_L < 500$ Mpc, $\nu L_\nu(\mathbf{6,AGN}) < 7 \times 10^{42}$ erg/s. Despite the low S/N of the spectra, here the result of the comparison is $F_{SB} = 4.6 \pm 0.8$ i.e. stronger SF activity in NLS1s. The statistics is good for NLS1s while there is only one BLS1s. Again the faintness of sources and low S/N prevent from the detection of broad optical emitting lines.

Zone B1: $D_L < 100$ Mpc, $7 \times 10^{42} < \nu L_\nu(\mathbf{6,AGN}) < 7 \times 10^{43}$ erg/s. Similarly to zone A2, the SF activity is enhanced in NLS1 ($F_{SB} = 8.2 \pm 0.4$) even if we have to take in mind the low BLS1 statistics.

Zone B2: $100 < D_L < 500$ Mpc, $7 \times 10^{42} < \nu L_\nu(\mathbf{6,AGN}) < 7 \times 10^{43}$ erg/s. As shown in Fig. 6, the $6.2 \mu\text{m}$ PAH feature appears more prominent in the NLS1 mean spectrum than in the BLS1 one, and this is also confirmed by the relative importance of star formation $F_{SB} = 2.8 \pm 0.2$.

Zone B3: $D_L > 500$ Mpc, $7 \times 10^{42} < \nu L_\nu(\mathbf{6,AGN}) < 7 \times 10^{43}$ erg/s. The low signal-to-noise of the data (lower-right panel of Fig. 6) reflects the faintness of the sources. Indeed we just compute a 3σ lower limit for the comparison parameter $F_{SB} > 0.5$. Nevertheless, we note that the $6.2 \mu\text{m}$ PAH feature is detected in the NLS1 stacked spectrum.

Zone C1: $D_L < 100$ Mpc, $7 \times 10^{43} < \nu L_\nu(\mathbf{6,AGN}) < 7 \times 10^{44}$ erg/s. A visual comparison of the data in upper-left panel of Fig. 6 does not allow to assign an enhanced SF activity to NLS1, but it is found from the comparison parameter $F_{SB} = 2.2 \pm 0.2$. Despite the low statistics, the significance of the result is preserved by the high S/N and quality of the data.

Zone C2: $100 < D_L < 500 \text{ Mpc}$, $7 \times 10^{43} < \nu L_\nu(\mathbf{6,AGN}) < 7 \times 10^{44} \text{ erg/s}$. There are 10 NLS1s and 11 BLS1s in this intermediate distance zone. The proper panel of Fig. 6 indicates a more intense $6.2 \mu\text{m}$ PAH feature in the mean NLS1 spectrum. The high statistics allows an accurate measurement of the SF comparison parameter: $F_{SB} = 5.9 \pm 0.4$.

Zone C3: $D_L > 500 \text{ Mpc}$, $7 \times 10^{43} < \nu L_\nu(\mathbf{6,AGN}) < 7 \times 10^{44} \text{ erg/s}$. The middle-right panel (Fig. 6) shows the stacked spectra from 5 and 16 NLS1 and BLS1, respectively. All the sources involved in the stacking are bright PG quasars (Boroson & Green 1992), and this nature reflects in the strong PAH dilution caused by the AGN continuum. PAH features are detected in both mean spectra, and a more intense SF activity is revealed in NLS1, ($F_{SB} = 1.8 \pm 0.3$).

Zone D2: $100 < D_L < 500 \text{ Mpc}$, $\nu L_\nu(\mathbf{6,AGN}) > \times 10^{44} \text{ erg/s}$. As in the case of zones A1 and C1, the statistics for both NLS1 and BLS1 is limited (respectively 1 and 2 sources). The $6.2 \mu\text{m}$ PAH feature is detected in the NLS1 spectrum, even if the quasar emission dilutes the line. On the contrary, in the BLS1 mean data the PAH feature is undetected. The corresponding lower limit for the comparison parameter is: $F_{SB} > 20$ with high significance given the limiting R upper limit ($R < 0.001$).

Zone D3: $D_L > 500 \text{ Mpc}$, $\nu L_\nu(\mathbf{6,AGN}) > 7 \times 10^{44} \text{ erg/s}$. The most distant and luminous sources lie in this region. The statistics are good (6 NLS1s, 12 BLS1s), and the data have very good signal-to-noise. PHL 1092 is the most distant source in the entire sample (an isolate red point in D3 bin of Fig. 5), and its SL observed spectrum does not cover the entire rest wavelength range, reaching only $\lambda_{rest} \sim 11 \mu\text{m}$. As a consequence, the stacked NLS1 spectrum is distorted beyond $\lambda_{rest} \sim 11 \mu\text{m}$. In the top-right panel of Fig. 6 we plot the mean NLS1 spectrum obtained without PHL 1092 in order to show a more correct mean continuum shape for this zone. This choice does not affect the shorter wavelength spectrum and the result on relative importance of star formation (R values calculated with and without PHL 1092 in the mean spectrum are consistent within the errors). The relative importance of star formation in zone D3 reaches the highest value ($F_{SB} = 24 \pm 9$) supporting the main conclusion of this paper.

8. Appendix B: peculiar sources

- Mrk 335 (Fig. 2) is a well characterized NLS1, but its mid-IR spectrum has no PAH features at all. Only a putative $7.7 \mu\text{m}$ PAH can be noticed, but it is distorted by a shallow Silicate absorption features centered at $9.7 \mu\text{m}$, thus we can not confirm its detection. The

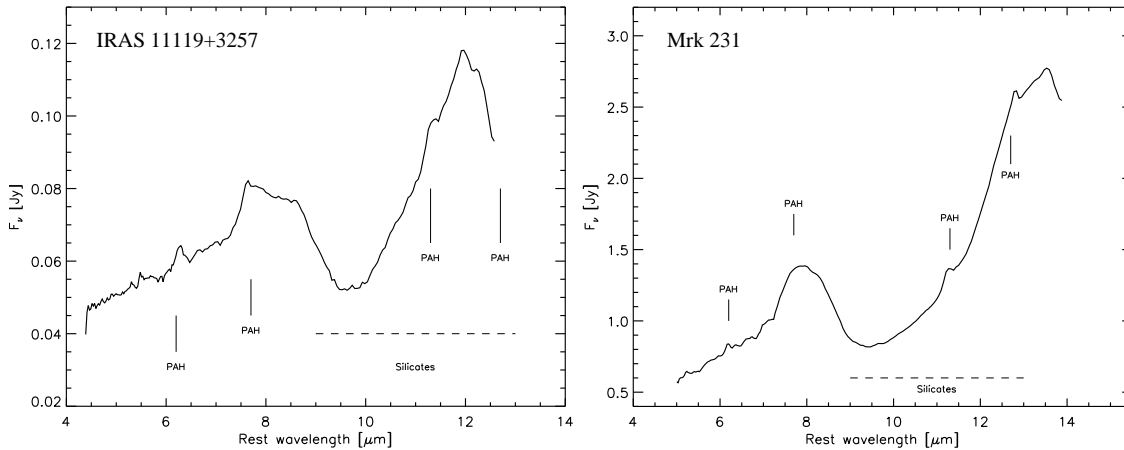


Fig. 10.— Low Resolution mid-IR spectra of IRAS 11119+3257 and Mrk 231 showing the very strong $9.7 \mu\text{m}$ silicate absorption feature.

shape of the Mrk 335 spectrum resembles that of quasars without PAH detections analyzed by S06. In that work the authors demonstrate that averaging 15 spectra similar to Mrk 335 the 7.7 and $11.3 \mu\text{m}$ PAH peaks are detected on the top of the strong AGN continuum. The result leaves open the possibility that a modest circumnuclear SF activity is actually present in Mrk 335 but the PAH features are strongly diluted by the AGN emission and lie under our detection capability.

- Among the archival samples there are three peculiar sources. Two of them ($5\text{-}15 \mu\text{m}$ spectra are shown in Figure 10), are the only objects showing a strong $9.7 \mu\text{m}$ silicate absorption: a NLS1 (IRAS 11119+3257) and a BLS1 (Mrk 231), both characterized by ULIRG infrared emission.

Mrk 231 is a well known low-ionization broad absorption line quasar (lo-BAL QSO), with a broad line region optically detectable even if the nucleus is heavily obscured in X-rays (Gallagher et al. 2005). Its MIR spectrum shows not only the silicate absorption related to such an absorbed ULIRG, but also a luminous $6.2 \mu\text{m}$ PAH emission ($L(6.2, \text{PAH}) \sim 3 * 10^{42} \text{erg/s}$) pointing out a significant starburst, even if not dominant ($R = 0.17 * 10^{-2}$). From the comparison of their low resolution spectra, IRAS 11119+3257 appears as the optical narrow line counterpart of Mrk 231. The only difference being the relative intensity of the Starburst, which in IRAS 11119+3257 is about twice the Mrk 231 values.

Even if it is not statistically significant, this coincidence is at least intriguing and may suggest a possible connection between NLS1 and lo-BAL quasars. Previous works support this suggestion: for example Brandt and Gallagher (2000) argued that the potential physical connection between NLS1s and lo-BAL QSOs is their high accretion rate close to the Eddington

limit. Also Zheng et al. (2002) found common physical conditions (Fe II strength, [O III] weakness, strong outflows) in NLS1s, lo-BAL QSOs and IR QSOs and ascribed differences between them to different viewing angles and/or from different evolution phases.

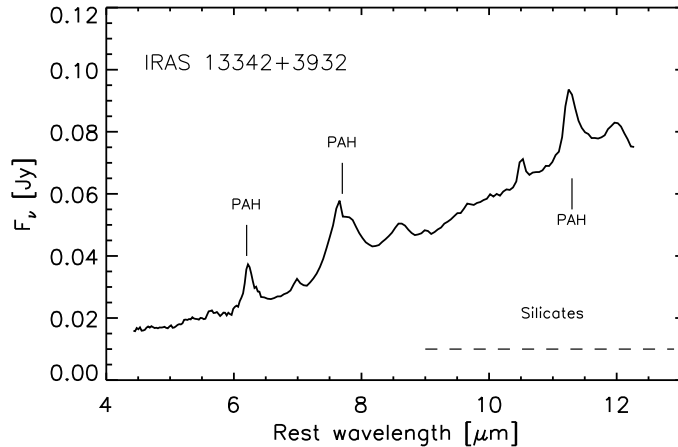


Fig. 11.— Low Resolution mid-IR spectrum of IRAS 13342+3932, an optically classified BLS1 showing very strong PAH emission features.

The third peculiar source in the archival sample is IRAS 13342+3932, another ULIRG galaxy, which is the only BLS1 showing strong 6.2 PAH emission. Even if its optical spectrum is typical of a pure type 1 Seyfert, the mid-IR one (Fig. 11) is Starburst dominated with an AGN infrared contribution $\sim 15\%$ (Weedman & Houck 2008). The fact that only one BLS1 is found with such a starburst dominated spectrum does not change our overall result about an enhanced star formation in NLS1 galaxies.

9. Acknowledgments

We thank the referee for helpful comments. We also thank Nico Hamaus for help with part of the initial data reduction.

Funding for this work at Tel Aviv University has been provided by the Israel Science Foundation grant 364/07 and the a DIP grant 15981.

NLS1					BLS1				
Source Name	z	D_L	FWHM(H_β)	Log λL_{5100}	Source Name	z	D_L	FWHM(H_β)	Log λL_{5100}
(1)	(2)	(3)	(4)	(5)	(1)	(2)	(3)	(4)	(5)
Ark 564	0.0247	108	865 ¹	44.12 ²	Fairall 9	0.0470	208	6690 ⁷	43.92 ⁷
IRAS 13224-3809	0.0667	300	650 ³	44.81 ²	IRAS 13342+3932	0.1790	866	7090 ⁷	44.42 ⁷
1H 0707-495	0.0411	181	1000 ¹	43.48 ⁴	FBS 0732+396	0.1180	550	2370 ⁷	44.31 ⁷
Ton S180	0.0620	278	1090 ⁶	44.71 ²	J095504.55+170556.3	0.139	656	2460 ⁷	43.80 ⁷
Mrk 1044	0.0165	72	1310 ¹	44.53 ²	J130842.24+021924.4	0.1400	661	5720 ⁷	43.86 ⁷
Mrk 335	0.0258	113	2081 ⁷	43.74 ⁷	J131305.68-021039.2	0.0837	381	4190 ⁷	43.86 ⁷
Mrk 359	0.0174	75	900 ¹	43.73 ²	J141556.84+052029.5	0.1260	590	4130 ⁷	44.00 ⁷
Mrk 896	0.0264	115	1135 ¹	43.95 ²	IRAS F14463+3612	0.1130	525	2100 ⁷	44.08 ⁷
Mrk 766	0.0129	56	1100 ⁶	43.57 ²	Mrk 836	0.0388	171	7180 ⁷	43.14 ⁷
NGC 4051	0.0023	10	1170 ¹	42.26 ²	J152139.66+033729.2	0.1260	590	7310 ⁷	43.14 ⁷
PHL 1092	0.3920	2150	1300 ¹	44.45 ⁴	J163631.29+420242.6	0.0610	273	7810 ⁷	43.47 ⁷
PG 1244+026	0.0482	214	1270 ⁷	43.59 ⁷	PG 0052+251	0.1550	739	5297 ⁷	44.78 ⁷
RE J1034+393	0.0424	187	1050 ⁷	43.26 ⁷	J171902.28+593715.9	0.1680	808	2250 ⁷	44.16 ⁷
Mrk 1239	0.0199	86	910 ³	43.72 ²	PG 1202+281	0.1650	792	6570 ⁷	44.20 ⁷
Mrk 957	0.0711	321	685 ³	43.55 ⁴	Mrk 1146	0.0389	172	2700 ⁷	43.28 ⁷
Mrk 507	0.0559	250	960 ³	44.25 ²	Mrk 590	0.0265	116	7110 ⁷	43.87 ⁷
Mrk 291	0.0352	155	2200 ⁷	43.25 ⁷	IRAS 07598+6508	0.1480	703	3150 ¹⁰	45.22 ²
Mrk 493	0.0313	137	1250 ⁷	43.37 ⁷	VII Zw 244	0.1310	615	2950 ⁷	44.14 ⁷
PG 1448+273	0.0650	292	1060 ⁷	44.28 ⁷	Mrk 106	0.1230	575	4420 ⁷	44.51 ⁷
Mrk 705	0.0292	128	2270 ⁷	43.26 ⁷	Mrk 1298	0.0600	269	2380 ⁷	43.80 ⁷
KUG 0301+002	0.0445	197	1460 ⁷	43.11 ⁷	Ton 1542	0.0640	287	3470 ⁷	43.90 ⁷
J082912.67+500652.3	0.0434	192	1080 ⁷	42.88 ⁷	NGC 4593	0.0090	39	5040 ⁷	42.62 ⁷
J024912.86-081525.6	0.0294	129	920 ⁷	44.33 ⁷	Mrk 231	0.0427	189	3130 ⁷	45.05 ⁷
IRAS 04312+4008	0.0205	89	690 ⁸	44.36 ⁸	Ton 730	0.0870	397	3480 ⁷	43.93 ⁷
Mrk 110	0.0353	155	1900 ⁷	43.01 ⁷	Mrk 279	0.0305	134	5000 ¹⁴	43.06 ⁴
J131305.80+012755.9	0.0294	128	2200 ⁷	43.84 ⁷	PG 1415+451	0.1140	530	2970 ⁷	44.18 ⁷
J094310.12+604559.1	0.0743	336	1100 ⁷	43.02 ⁷	PG 1519+226	0.1370	646	2380 ⁷	44.40 ⁷
Mrk 142	0.0450	199	1750 ⁷	43.57 ⁷	PG 2209+184	0.0700	316	6690 ⁷	43.69 ⁷
Mrk 42	0.0246	107	940 ⁷	42.84 ⁷	III Zw 2	0.0893	408	4820 ⁷	44.41 ⁷
J142748.28+050222.0	0.1060	490	1470 ⁷	44.26 ⁷	Mrk 141	0.0417	184	4910 ⁷	43.50 ⁷
IC 3599	0.0215	94	670 ⁷	42.40 ⁷	PG 1149-110	0.0490	218	2920 ⁷	43.66 ⁷
J170246.09+602818.9	0.0690	311	1980 ⁷	43.14 ⁷	IC 4329A	0.0160	69	5930 ⁷	43.17 ⁷
J114008.71+030711.4	0.0811	368	550 ⁷	43.24 ⁷	PG1416-129	0.1290	605	6885 ⁷	44.12 ⁷
J145047.19+033645.4	0.0670	302	1800 ⁷	42.99 ⁷	PG 2304+042	0.0420	186	8390 ⁷	43.59 ⁷
J124035.81-002919.4	0.0810	368	1000 ⁷	43.33 ⁷	J151653.22+190048.2	0.1900	926	4840 ¹⁵	44.20 ⁴
J125055.28-015556.8	0.0814	370	620 ⁷	43.24 ⁷	PG 0804+761	0.1000	460	3085 ⁷	44.60 ⁷
J135724.52+652505.8	0.1060	490	1240 ⁷	43.28 ⁷	PG 0923+201	0.1900	926	6140 ⁷	45.06 ⁷
J141234.68-003500.0	0.1270	595	1150 ⁷	43.44 ⁷	PG 1411+442	0.0896	410	2850 ⁷	44.31 ⁷
J144507.30+593649.9	0.1280	600	1960 ⁷	43.03 ⁷	PG 1626+554	0.1320	620	4270 ⁷	44.45 ⁷
IRAS 15462-0450	0.0998	459	1615 ¹⁰	43.96 ²	PG 1048+382	0.1670	802	3550 ⁷	44.49 ⁷
J172759.15+542147.0	0.0995	458	1380 ⁷	43.03 ⁷	PG 1114+445	0.1440	682	5300 ⁷	44.76 ⁷
I Zw 1	0.0611	274	1240 ¹	44.63 ⁹	PG 0844+349	0.0640	287	2300 ⁷	43.97 ⁷
PG 1211+143	0.0809	368	1860 ⁵	45.00 ²	PG 1116+215	0.1770	856	3530 ⁷	45.13 ⁷
PKS 0558-504	0.1370	646	1250 ¹	44.15 ⁴	Mrk 1383	0.0865	395	6620 ⁷	44.45 ⁷
IRAS11119+3257	0.1890	920	1980 ¹⁰	45.67 ¹⁰	PG 1435-067	0.1260	590	3180 ⁷	43.39 ⁷
IRAS13349+2438	0.1080	500	2800 ¹	44.64 ⁶	Mrk 876	0.1290	605	8810 ⁷	44.67 ⁷
PG1404+226	0.0980	450	1390 ⁷	44.18 ⁷	Mrk 877	0.1140	530	5940 ⁷	44.25 ⁷
Mrk 478	0.0770	349	1450 ⁷	44.21 ⁷	Mrk 304	0.0658	296	5700 ⁷	44.41 ⁷
PHL 1811	0.1920	936	1500 ¹¹	44.97 ⁴	PG1322+659	0.1680	808	2850 ⁷	44.51 ⁷
PG 0026+149	0.1450	687	1860 ⁵	44.96 ⁵	PG 1151+117	0.1770	856	4770 ⁷	44.70 ⁷
PG 1402+261	0.1640	786	2040 ⁷	44.30 ⁷	PG1307+085	0.1550	739	4380 ⁷	44.78 ⁷
PG 1115+047	0.1550	739	1860 ⁷	44.15 ⁷	PG1309+355	0.1840	893	4910 ⁷	45.08 ⁷
PG 1001+054	0.1600	765	1790 ⁷	44.55 ⁷	IRAS 21219-1757	0.1130	525	2080 ¹⁰	44.23 ¹⁰
PG 2130+099	0.0620	278	2800 ⁷	44.26 ⁷	PKS 2349-01	0.1740	840	5480 ⁷	44.82 ⁷
IRAS 03450+0055	0.0310	136	1310 ⁸	43.00 ⁸	PG1012+008	0.1870	909	3220 ⁷	44.63 ⁷
PG 1011-040	0.0580	259	1440 ⁵	44.30 ⁵					
Mrk 734	0.0502	223	2200 ⁷	43.88 ⁷					
Mrk 486	0.0389	172	1730 ⁷	43.59 ⁷					
IRAS 20237-1547	0.1920	936	1570 ¹⁰	47.15 ¹⁰					
ESO 323-G077	0.0149	64	2100 ¹²	42.94 ¹³					
PG 1552+085	0.1190	555	1670 ⁷	44.43 ⁷					

Table 1: Overall properties of the complete sample. Columns: (1) source name; sources labeled with only the J2000 coordinates are from the SDSS catalog. The first 20 line in the NLS1 dedicated panel correspond to our original sample. (2) redshift. (3) Luminosity distance in Mpc for a $H_0 = 70 \text{ km s}^{-1} \text{Mpc}^{-1}$, $\Omega_m = 0.3$ and $\Omega_\Lambda = 0.7$ cosmology. (4)-(5) H_β FWHM (km/s) and 5100 Å continuum luminosity (erg s^{-1}) with related references. References: ¹ Gallo 2006, ² Hao et al. 2005, ³ Boller et al. 1996, ⁴ Véron-Cetty & Véron 2006, ⁵ Boroson & Green 1992, ⁶ Grupe et al. 2004, ⁷ this work: the electronically available optical spectra (i.e. SDSS sources and PG quasars) have been fitted consistently with NT07 §2.2., ⁸ Véron-Cetty & Véron 2001, ⁹ Zhou et al. 2006, ¹⁰ Zheng et al. 2002, ¹¹ Whalen et al. 2006, ¹² Schmid et al. 2003, ¹³ Mulchaey et al. 1996, ¹⁴ Boroson & Meyers 1992, ¹⁵ Smith et al. 2003

NLS1					BLS1				
Source Name (1)	PID (2)	Date (3)	Int. Time (4)	Ref (5)	Source Name (1)	PID (2)	Date (3)	Int. time (4)	Ref (5)
Ark 564	20241	2005 Dec. 17	14x5	1	Fairall 9	30572	2007 Jun. 16	14x2	1
IRAS 13224-3809	20241	2005 Jul. 04	14x5	1	IRAS 13342+3932	00105	2004 May. 13	60x2	4
1H 0707-495	20241	2006 Nov. 15	14x5	1	FBS 0732+396	20741	2006 Apr. 23	14x4	1
Ton S180	20241	2005 Jul. 08	14x5	1	J095504.55+170556.3	00049	2004 Apr.19	14x2	2
Mrk 1044	20241	2005 Aug. 04	14x5	1	J130842.24+021924.4	20741	2006 Jan. 28	14x4	1
Mrk 335	20241	2005 Jul. 08	14x5	1	J131305.68-021039.2	20741	2006 Jan. 31	14x4	1
Mrk 359	20241	2006 Jan. 15	14x5	1	J141556.84+052029.5	20741	2006 Mar. 09	14x4	1
Mrk 896	20241	2005 Nov. 20	14x5	1	IRAS F14463+3612	40991	2007 Jun. 20	60x1	1
Mrk 766	20241	2006 Jun. 22	14x5	1	Mrk 836	20741	2006 Jan. 27	14x4	1
NGC 4051	20241	2005 Dec. 11	14x5	1	J152139.66+033729.2	20741	2005 Aug. 13	14x4	1
PHL 1092	20241	2006 Jan. 15	14x5	1	J163631.29+420242.6	20741	2005 Aug. 15	14x4	1
PG1244+026	20241	2005 Jul. 02	14x5	1	PG1416-129	20142	2005 Aug. 15	60x2	3
RE J1034+393	20241	2005 Dec. 16	14x5	1	J171902.28+593715.9	40038	2007 Jun. 15	60x2	1
Mrk 1239	20241	2006 Dec. 19	14x5	1	PG0052+251	00082	2004 Jan. 04	14x1	6
Mrk 957	20241	2006 Jan. 01	14x5	1	Mrk 1146	20741	2006 Jan. 15	14x4	1
Mrk 507	20241	2005 Jul. 01	14x5	1	Mrk 590	00086	2006 Jan. 20	14x2	3
Mrk 291	20241	2005 Aug. 13	14x5	1	IRAS 07598+6508	00105	2004 Feb. 29	14x3	4
Mrk 493	20241	2005 Aug. 15	14x5	1	VII Zw 244	03187	2005 Nov. 14	60x2	5
PG 1448+273	20241	2005 Jul. 01	14x5	1	Mrk 106	20741	2006 May. 20	14x4	1
Mrk 705	20241	2006 May. 28	14x5	1	Mrk 1298	03187	2005 Jul. 01	60x2	5
KUG 0301+002	20741	2006 Sep. 09	14x4	1	Ton 1542	03187	2005 Jul. 07	60x2	5
J082912.67+500652.3	20741	2006 Apr. 24	14x4	1	NGC 4593	00086	2005 Jul. 02	14x2	3
J024912.86-081525.6	30119	2007 Feb. 09	60x2	1	Mrk 231	00105	2004 Apr. 14	14x2	4
IRAS 04312+4008	30715	2007 Mar. 24	14x4	1	Ton 730	20142	2006 Jan. 19	60x2	3
Mrk 110	20142	2006 May. 20	60x2	3	Mrk 279	00666	2003 Nov. 16	14x1	8
J131305.80+012755.9	20741	2006 Jan. 28	14x4	1	PG 1415+451	20142	2006 Jan. 18	60x2	3
J094310.12+604559.1	20741	2006 May. 20	14x4	1	PG 1519+226	20142	2005 Aug. 13	60x2	3
Mrk 142	20142	2006 May. 27	60x2	3	PG 2209+184	20142	2006 Jun. 25	60x2	3
Mrk 42	30715	2007 Jun. 14	60x8	1	III Zw 2	00086	2005 Jul. 10	14x2	3
J142748.28+050222.0	20741	2006 Jul. 24	14x4	1	Mrk 141	20741	2005 Nov. 15	14x4	1
IC 3599	30715	2006 Jun. 24	60x4	1	PG 1149-110	20142	2005 Aug. 13	60x2	3
J170246.09+602818.9	30119	2006 Aug. 07	60x2	1	IC 4329A	00086	2004 Jul. 13	14x2	3
J114008.71+030711.4	30119	2007 Jun. 11	14x7	1	PG1202+281	20142	2006 Jun. 22	60x2	3
J145047.19+033645.4	20741	2005 Aug. 15	14x4	1	PG 2304+042	20142	2005 Dec. 17	60x2	3
J124035.81-002919.4	20741	2005 Jul. 14	14x4	1	J151653.22+190048.2	00049	2004 Apr. 01	14x1	2
J125055.28-015556.8	30119	2006 Jul. 24	14x7	1	PG 0804+761	00014	2004 Mae. 02	14x3	4
J135724.52+652505.8	30119	2006 Dec. 23	60x2	1	PG 0923+201	03187	2005 Nov. 12	60x2	5
J141234.68-003500.0	30119	2006 Jul. 24	14x7	1	PG 1411+442	03187	2005 Jan. 11	60x2	5
J144507.30+593649.9	30119	2006 Dec. 23	60x2	1	PG 1626+554	03187	2005 Jan. 08	60x5	5
IRAS 15462-0450	00105	2004 Mar. 03	60x1	4	PG 1048+382	20142	2006 Jan. 31	60x2	3
J172759.15+542147.0	30119	2006 Aug. 04	60x2	1	PG 1114+445	20142	2006 May. 07	60x2	3
I Zw 1	00014	2004 Jan. 07	14x2	4	PG 0844+349	03187	2005 Nov. 14	60x2	5
PG 1211+143	00014	2004 Jan. 08	14x3	4	PG 1116+215	00082	2004 May. 14	6x1	6
PKS 0558-504	00082	2004 Mar. 27	14x1	1	Mrk 1383	03187	2005 Feb. 13	60x2	5
IRAS 11119+3257	00105	2004 May. 13	60x1	4	PG 1435-067	03187	2007 Jul. 12	60x2	5
IRAS 13349+2438	00061	2005 Jun. 07	14x5	7	Mrk 876	03187	2004 Nov. 15	60x2	5
PG1404+226	20142	2006 Mar. 05	60x2	3	Mrk 877	03187	2005 Mar. 15	60x3	5
Mrk 478	03187	2005 Jan. 14	60x2	5	Mrk 304	03187	2004 Nov. 15	60x3	5
PHL 1811	30426	2006 Nov. 12	14x2	1	PG 1322+659	20142	2006 Jun. 21	60x2	3
PG 0026+149	03187	2005 Aug. 11	240x4	5	PG 1151+117	00082	2003 Dec. 18	6x1	6
PG 1402+261	00082	2004 Jun. 08	14x1	6	PG1307+085	00082	2006 Jan. 19	6x1	3
PG 1115+047	20142	2006 May. 27	60x2	3	PG1309+355	00082	2004 May. 14	6x1	6
PG 1001+054	03187	2005 May. 23	240x2	5	IRAS 21219-1757	03187	2004 Nov. 16	60x2	5
PG 2130+099	00014	2004 Jun. 06	14x3	4	PKS 2349-01	03187	2004 Dec. 13	60x3	5
IRAS 03450+0055	00082	2004 Aug. 31	6x1	7	PG1012+008	20142	2006 dec. 19	14x7	3
PG 1011-040	20142	2006 Jun. 23	60x2	3					
Mrk 734	00014	2004 May. 13	14x3	4					
Mrk 486	03421	2005 Jan. 06	60x3	9					
IRAS 20237-1547	00105	2004 Apr. 19	60x2	4					
ESO 323-G077	30745	2006 Aug. 06	14x2	1					
PG 1552+085	20142	2005 Aug. 13	60x2	3					

Table 2: Observation log. Columns: (1) Source Name. (2) Proposal identification code. (3) Observation Date. (4) Exposure Time (ramp duration in sec per number of cycles). (5) First publication of the IRS/Spitzer low resolution data: 1. This work, 2. Shy et al. 2007, 3. Shy et al. 2006, 4. Hao et al. 2005, 5. Schweitzer et al. 2006, 6. Maiolino et al. 2007, 7. Thompson et al. 2009, 8. Dasyra et al. 2008, 9. Cao et al. 2008.

NLS1						BLS1					
Source Name (1)	f_ν (AGN) (2)	F_{PAH} (3)	νL_ν (AGN) (4)	L_{PAH} (5)	R (6)	Source Name (1)	f_ν (AGN) (2)	F_{PAH} (3)	νL_ν (AGN) (4)	L_{PAH} (5)	R (6)
Ark 564	67.6	<0.31	4.70	<0.043	<0.09	Fairall 9	159	<0.74	41.2	<0.39	<0.09
IRAS 13224-3809	17.8	2.01 ± 0.08	9.58	2.17	2.26	IRAS 13342+3932	20.2	2.16 ± 0.06	90.6	19.4	2.15
1H 0707-495	10.0	<0.33	1.97	<0.13	<0.66	FBS 0732+396	26.5	<0.20	47.9	<0.71	<0.15
Ton S180	4.7	<0.62	2.17	<0.58	<2.66	J095504.55+170556.3	6.8	<0.78	17.5	<4.0	<2
Mrk 1044	50.9	1.81 ± 0.12	1.56	0.11	0.71	J130842.24+021924.4	1.0	<0.35	2.62	<1.8	<0.7
Mrk 335	108.9	<0.53	8.27	<0.080	<0.10	J131305.68-021039.2	5.5	0.29 ± 0.08	4.77	0.51	1.1
Mrk 359	28.8	2.50 ± 0.14	0.98	0.17	1.34	J141556.84+052029.5	1.9	<0.37	3.95	0.15	<3.9
Mrk 896	27.4	1.38 ± 0.06	2.18	0.22	1.01	IRAS F14463+3612	9.5	<0.16	15.6	<0.51	<0.33
Mrk 766	97.4	4.99 ± 0.16	1.81	0.19	1.03	Mrk 836	3.8	<0.33	0.66	<0.12	<1.8
NGC 4051	144	6.9 ± 0.3	0.084	0.008	0.96	J152139.66+033729.2	7.5	<0.21	15.6	<0.90	<0.6
PHL 1092	10.5	<0.35	289	<19	<0.67	J163631.29+420242.6	2.6	<0.37	1.16	<0.33	<2.8
PG1244+026	17.7	0.25 ± 0.08	48.5	0.14	0.29	PG1416-129	7.9	0.12 ± 0.04	17.3	0.51	0.30
RE J1034+393	30.1	1.3 ± 0.1	6.33	0.56	0.88	J171902.28+593715.9	6.1	<0.12	23.8	<0.9	<0.4
Mrk 1239	361	2.5 ± 0.3	16.2	0.23	0.14	PG0052+251	21.5	<0.76	70.2	<5.0	<0.71
Mrk 957	10.5	3.74 ± 0.12	6.46	4.62	7.14	Mrk 1146	14.9	0.47 ± 0.06	2.62	0.17	<0.63
Mrk 507	12.7	2.38 ± 0.14	4.73	1.77	3.75	Mrk 590	30.2	<0.23	2.42	<0.04	<0.2
Mrk 291	4.0	1.76 ± 0.06	0.57	0.50	8.79	IRAS 07598+6508	162.5	0.90 ± 0.14	480	5.30	0.11
Mrk 493	32.9	2.59 ± 0.08	3.71	0.58	1.58	VII Zw 244	11.5	0.12 ± 0.04	26.0	0.53	0.20
PG 1448+273	19.9	<0.27	10.2	<0.28	<0.27	Mrk 106	114	<0.47	225	<1.9	<0.08
Mrk 705	42.2	1.48 ± 0.08	4.13	0.29	0.70	Mrk 1298	42.1	0.33 ± 0.04	18.2	0.29	0.16
KUG 0301+002	6.4	0.43 ± 0.08	1.49	0.20	1.34	Ton 1542	28.3	<0.12	14.0	<0.12	<0.08
J082912.67+500652.3	2.1	0.3 ± 0.1	0.46	0.13	2.79	NGC 4593	150.8	1.6 ± 0.2	1.36	0.03	0.21
J024912.86-081525.6	0.4	<0.18	0.04	0.03	<8.8	Mrk 231	746	6 ± 1	159	2.65	0.17
IRAS 04312+4008	4.17	8.7 ± 0.2	1.98	0.83	4.17	Ton 730	10.2	<0.14	9.61	0.26	0.27
Mrk 110	36.5	0.16 ± 0.02	90.6	0.04	0.005	Mrk 279	76.7	0.8 ± 0.2	8.20	0.16	0.2
J131305.80+012755.9	1.1	<0.31	0.11	<0.06	<5.7	PG 1415+451	16.4	0.27 ± 0.02	27.5	0.92	0.33
J094310.12+604559.1	18.0	<0.19	12.2	<0.26	<0.22	PG 1519+226	23.4	0.14 ± 0.04	58.4	0.68	0.12
Mrk 142	12.2	0.99 ± 0.04	2.90	0.47	1.63	PG 2209+184	10.1	0.33 ± 0.04	6.02	0.40	0.66
Mrk 42	7.6	1.46 ± 0.04	0.52	0.20	3.85	III Zw 2	39.8	<0.49	39.6	<0.47	<0.25
J142748.28+050222.0	4.2	<0.2	6.03	<0.56	<0.93	Mrk 141	21.3	1.4 ± 0.1	43.3	0.58	1.34
IC 3599	3.5	0.47 ± 0.02	0.18	0.05	2.68	PG 1149-110	16.6	0.12 ± 0.04	4.70	0.07	0.14
J170246.09+602818.9	0.6	0.08 ± 0.02	0.35	0.09	2.60	IC 4329A	486	1.72 ± 0.03	14.0	0.10	0.07
J114008.71+030711.4	1.2	0.37 ± 0.06	0.97	0.60	6.18	PG1202+281	14.9	0.14 ± 0.02	55.8	1.02	0.18
J145047.19+033645.4	<0.6	<0.21	<0.33	<0.23	-	PG 2304+042	9.2	<0.14	1.89	<0.06	<0.3
J124035.81-002919.4	4.6	<0.29	3.73	<0.47	<1.3	J151653.22+190048.2	70.2	<1.3	360	<14	<0.4
J125055.28-015556.8	0.7	<0.27	0.57	<0.45	<7.8	PG 0804+761	94.0	<0.29	119	<0.74	<0.06
J135724.52+652505.8	1.1	<0.18	15.8	<0.50	<3.2	PG 0923+201	25.5	<0.21	131	<2.20	<0.2
J141234.68-003500.0	1.0	<0.29	2.12	<1.24	<5.9	PG 1411+442	60.4	<0.25	60.6	<0.51	<0.08
J144507.30+593649.9	0.4	<0.10	0.86	<0.42	<4.9	PG 1626+554	11.3	0.12 ± 0.02	26.0	0.54	0.21
IRAS 15462-0450	32.9	2.32 ± 0.08	41.5	5.86	1.41	PG 1048+382	7.4	0.10 ± 0.02	28.5	0.75	0.26
J172759.15+542147.0	0.7	<0.10	0.88	<0.25	<2.8	PG 1114+445	35.2	<0.12	97.9	<0.65	<0.07
I Zw 1	187	1.62 ± 0.18	83.9	1.45	0.17	PG 0844+349	27.0	<0.18	13.3	<0.17	<0.13
PG 1211+143	72.8	<0.55	58.8	<0.88	<0.15	PG 1116+215	59.0	<0.70	258	<6.2	<0.24
PKS 0558-504	23.8	0.66 ± 0.18	59.4	3.31	0.56	Mrk 1383	55.6	0.18	51.7	<0.33	<0.06
IRAS 11119+3257	56.2	0.84 ± 0.08	285	8.50	0.30	PG 1435-067	17.8	<0.14	37.0	<0.57	<0.15
IRAS 13349+2438	321	<0.45	47.9	<1.34	<0.03	Mrk 876	53.4	1.01 ± 0.04	117	4.45	0.38
PG 1404+226	9.0	0.16 ± 0.02	10.9	0.38	0.35	Mrk 877	24.5	<0.12	41.1	<0.39	0.10
Mrk 478	51.2	1.21 ± 0.06	37.3	1.76	0.47	Mrk 304	55.1	<0.18	28.8	<0.18	<0.06
PHL 1811	58.7	0.45 ± 0.12	308	4.71	0.15	PG1322+659	15.9	0.18 ± 0.04	62.0	1.37	0.22
PG 0026+149	16.8	<0.10	47.4	<0.55	<0.12	PG 1151+117	10.5	<1.0	46.0	<8.9	<1.9
PG 1402+261	40.2	<0.35	149	<2.6	<0.18	PG1307+085	18.1	<1.3	59.1	<8.2	<1.4
PG 1115+047	13.7	0.43 ± 0.04	44.8	2.81	0.63	PG1309+355	25.5	<1.1	122	<10	<0.8
PG 1001+054	15.3	0.14 ± 0.04	53.6	0.96	0.18	IRAS 21219-1757	69.6	0.53 ± 0.08	115	1.73	0.15
PG 2130+099	87.2	<0.45	40.3	<0.42	<0.10	PKS 2349-01	23.2	0.16 ± 0.04	97.8	1.32	0.13
IRAS 03450+0055	93.5	<0.90	10.3	<0.20	<0.19	PG1012+008	17.3	<0.30	85.5	<2.9	<0.34
PG 1011-040	17.7	0.14 ± 0.04	7.11	0.11	0.16						
Mrk 734	37.8	0.4 ± 0.1	11.3	0.24	0.22						
Mrk 486	34.8	0.14 ± 0.04	6.13	0.05	0.08						
IRAS 20237-1547	34.7	1.93 ± 0.08	182	20.3	1.11						
ESO 323-G077	247	14.8 ± 0.4	6.15	0.74	1.2						
PG 1552+085	12.2	<0.10	22.4	<0.36	<0.16						

Table 3: Mid-IR spectral parameters. Columns: (1) source name; sources labeled only with J2000 coordinates are from the SDSS catalog. (2) AGN flux density at $6 \mu\text{m}$ in units of mJy. Sources with a $6 \mu\text{m}$ upper limit are nondetections at a 3σ level and are not included in the bidimensional plots. (3) $6.2 \mu\text{m}$ PAH flux in $10^{-20}\text{W}/\text{cm}^2$. (4) AGN $6 \mu\text{m}$ luminosity in 10^{43}erg/s . (5) PAH luminosity in 10^{42}erg/s . (6) SB/AGN luminosity ratio in units of 10^{-2} .

Zone	R (NLS1)	R (BLS1)	F_{SB}
A1	0.185 ± 0.003	-	-
A2	0.387 ± 0.012	0.085 ± 0.012	4.6 ± 0.8
B1	0.179 ± 0.002	0.022 ± 0.001	8.2 ± 0.4
B2	0.146 ± 0.004	0.052 ± 0.003	2.8 ± 0.2
B3	0.10 ± 0.02	< 0.2	> 0.5
C1	0.015 ± 0.001	0.007 ± 0.001	2.2 ± 0.2
C2	0.047 ± 0.01	0.008 ± 0.004	5.9 ± 0.4
C3	0.025 ± 0.001	0.014 ± 0.002	1.8 ± 0.3
D2	0.018 ± 0.001	< 0.001	> 20
D3	0.063 ± 0.001	0.003 ± 0.001	24 ± 9

Table 4: Star formation activity parameters for the ten stacking zones in Fig. 6: R and F_{SB} are shown with propagated errors. The error on F_{SB} are statistical, the dispersion of the data is not taken into account.

REFERENCES

- Brandt, W. N., & Gallagher, S. C. 2000, *New Astronomy Review*, 44, 461
- Boller, T., Brandt, W. N., & Fink, H. 1996, *A&A*, 305, 53
- Boroson, T. A., & Green, R. F. 1992, *ApJS*, 80, 109
- Boroson, T. A., & Meyers, K. A. 1992, *ApJ*, 397, 442
- Boroson, T. A. 2002, *ApJ*, 565, 78
- Cao, C., Xia, X. Y., Wu, H., Mao, S., Hao, C. N., & Deng, Z. G. 2008, *MNRAS*, 390, 336
- Chen, Y.-M., Wang, J.-M., Yan, C.-S., Hu, C., & Zhang, S. 2009, *ApJ*, 695, L130
- Corbin, M. R. 1997, *ApJS*, 113, 245
- Di Matteo, T., Springel, V., & Hernquist, L. 2005, *Nature*, 433, 604
- Fabian, A. C., et al. 2009, *Nature*, 459, 540
- Ferrarese, L., & Merritt, D. 2000, *ApJ*, 539, L9
- Gallagher, S. C., Schmidt, G. D., Smith, P. S., Brandt, W. N., Chartas, G., Hylton, S., Hines, D. C., & Brotherton, M. S. 2005, *ApJ*, 633, 71

- Gallo, L. C., Boller, T., Tanaka, Y., Fabian, A. C., Brandt, W. N., Welsh, W. F., Anabuki, N., & Haba, Y. 2004, *MNRAS*, 347, 269
- Gallo, L. C. 2006, *MNRAS*, 368, 479
- Gebhardt, K., et al. 2000, *ApJ*, 539, L13
- Genzel, R., et al. 1998, *ApJ*, 498, 579
- Grupe, D., Wills, B. J., Leighly, K. M., & Meusinger, H. 2004, *AJ*, 127, 156
- Grupe, D. 2004, *AJ*, 127, 1799
- Grupe, D., & Mathur, S. 2004, *ApJ*, 606, L41
- Hao, L., et al. 2005, *ApJ*, 625, L75
- Hao, C. N., Xia, X. Y., Mao, S., Wu, H., & Deng, Z. G. 2005, *ApJ*, 625, 78
- Higdon, S. J. U., et al. 2004, *PASP*, 116, 975
- Houck, J. R., et al. 2004, *ApJS*, 154, 18
- Kaspi, S., Maoz, D., Netzer, H., Peterson, B. M., Vestergaard, M., & Jannuzi, B. T. 2005, *ApJ*, 629, 61
- Kawakatu, N., & Wada, K. 2009, *ApJ*, 706, 676
- Lutz, D., et al. 2008, *ApJ*, 684, 853
- Maiolino, R., Shemmer, O., Imanishi, M., Netzer, H., Oliva, E., Lutz, D., & Sturm, E. 2007, *A&A*, 468, 979
- Marconi, A., & Hunt, L. K. 2003, *ApJ*, 589, L21
- Marconi, A., Risaliti, G., Gilli, R., Hunt, L. K., Maiolino, R., & Salvati, M. 2004, *MNRAS*, 351, 169
- Marziani, P., Sulentic, J. W., Zamanov, R., Calvani, M., Dultzin-Hacyan, D., Bachev, R., & Zwitter, T. 2003, *ApJS*, 145, 199
- Mathur, S. 2000, *MNRAS*, 314, L17
- Mathur, S., Kuraszkiewicz, J., & Czerny, B. 2001, *New Astronomy*, 6, 321
- Mulchaey, J. S., Wilson, A. S., & Tsvetanov, Z. 1996, *ApJS*, 102, 309

- Nardini, E., Risaliti, G., Salvati, M., Sani, E., Imanishi, M., Marconi, A., & Maiolino, R. 2008, MNRAS, 385, L130
- Netzer, H., & Trakhtenbrot, B. 2007, ApJ, 654, 754
- Netzer, H., et al. 2007, ApJ, 666, 806
- Netzer, H. 2009, ApJ, 695, 793
- Osterbrock, D. E., & Pogge, R. W. 1985, ApJ, 297, 166
- Pet, R. & Peto, J. 1972, Journal of the Royal Statistical Society, Series A (General) 135 (2): 185207
- Peterson, B. M., McHardy, I. M., & Wilkes, B. J. 2000, New Astronomy Review, 44, 491
- Risaliti, G., et al. 2006, MNRAS, 365, 303
- Rowan-Robinson, M. 1995, MNRAS, 272, 737
- Rowan-Robinson, M., & Efstathiou, A. 2009, MNRAS, 399, 615
- Schmid, H. M., Appenzeller, I., & Burch, U. 2003, A&A, 404, 505
- Shemmer, O., & Netzer, H. 2002, ApJ, 567, L19
- Shemmer, O., Netzer, H., Maiolino, R., Oliva, E., Croom, S., Corbett, E., & di Fabrizio, L. 2004, ApJ, 614, 547
- Shi, Y., et al. 2006, ApJ, 653, 127
- Shi, Y., et al. 2007, ApJ, 669, 841
- Silk, J., & Rees, M. J. 1998, A&A, 331, L1
- Smith, P. S., Schmidt, G. D., Hines, D. C., & Foltz, C. B. 2003, ApJ, 593, 676
- Spoon, H. W. W., Keane, J. V., Tielens, A. G. G. M., Lutz, D., Moorwood, A. F. M., & Laurent, O. 2002, A&A, 385, 1022
- Spoon, H. W. W., Marshall, J. A., Houck, J. R., Elitzur, M., Hao, L., Armus, L., Brandl, B. R., & Charmandaris, V. 2007, ApJ, 654, L49
- Sturm, E., et al. 2005, ApJ, 629, L21

- Tacconi, L. J., Genzel, R., Lutz, D., Rigopoulou, D., Baker, A. J., Iserlohe, C., & Tecza, M. 2002, *ApJ*, 580, 73
- Tanaka, Y., Boller, T., Gallo, L., Keil, R., & Ueda, Y. 2004, *PASJ*, 56, L9
- Thomas, H.-C., Beuermann, K., Reinsch, K., Schwobe, A. D., Truemper, J., & Voges, W. 1998, *A&A*, 335, 467
- Thompson, G. D., Levenson, N. A., Uddin, S. A., & Sirocky, M. M. 2009, *ApJ*, 697, 182
- Véron-Cetty, M.-P., Véron, P., & Gonçalves, A. C. 2001, *A&A*, 372, 730
- Véron-Cetty, M.-P., & Véron, P. 2006, *A&A*, 455, 773
- Whalen, D. J., Laurent-Muehleisen, S. A., Moran, E. C., & Becker, R. H. 2006, *AJ*, 131, 1948
- Weedman, D. W., & Houck, J. R. 2008, *ApJ*, 686, 127
- Zheng, X. Z., Xia, X. Y., Mao, S., Wu, H., & Deng, Z. G. 2002, *AJ*, 124, 18
- Zhou, H., Wang, T., Yuan, W., Lu, H., Dong, X., Wang, J., & Lu, Y. 2006, *ApJS*, 166, 128
- Zwicky, F., & Zwicky, M. A. 1971, *Guemligen: Zwicky*, —c1971,